Rock mass strength and elastic modulus of the Buntsandstein: An important lithostratigraphic unit for geothermal exploitation in the Upper Rhine Graben

Michael Heap, Marlène Villeneuve, Alexandra R.L. Kushnir, Jamie Farquharson, Patrick Baud, Thierry Reuschlé

Rock mass strength and elastic modulus of the Buntsandstein: an important lithostratigraphic unit for geothermal exploitation in the Upper Rhine Graben

Michael J. Heap[1]*, Marlène Villeneuve[2], Alexandra R.L. Kushnir[1], Jamie I. Farquharson[1,3], Patrick Baud[1], and Thierry Reuschlé[1]

[1]*Géophysique Expérimentale, Institut de Physique de Globe de Strasbourg (UMR 7516 CNRS, Université de Strasbourg/EOST), 5 rue René Descartes, 67084 Strasbourg cedex, France*

[2]*Department of Geological Sciences, University of Canterbury, Private Bag 4800, Christchurch, New Zealand.*

[3]*Department of Marine Geosciences, Rosenstiel School Of Marine And Atmospheric Sciences, University of Miami, 4600 Rickenbacker Causeway, Miami, United States of America*

*Corresponding author: heap@unistra.fr

Abstract

Geothermal exploitation in the Upper Rhine Graben increasingly targets the interface between the granitic basement and the overlying Buntsandstein unit. Results from deformation experiments are combined with structural assessments to provide reservoir-scale wet and dry strength and elastic modulus profiles for the Buntsandstein at Soultz-sous-Forêts (France). Our analysis finds five zones characterised by low strength and elastic modulus. The strength and elastic modulus of "massive" zones are lower when the rock is wet (i.e. water-saturated), highlighting the importance of performing wet deformation experiments for geothermal rock mass assessments. These data and methods can be used to provide assessments of other geothermal sites within the region to assist prospection, stimulation, and optimisation strategies.

Keywords: Buntsandstein; uniaxial compressive strength; triaxial deformation experiments; porosity; clay content; geothermal reservoir

Highlights

- Buntsandstein sandstone is of lower strength when wet.
- Water-weakening in sandstone is likely due to the presences of clays.
- Five low strength and stiffness zones exist within the Buntsandstein at Soultz.
- Wet experiments are important for geothermal rock mass assessments.
- Method presented can be adopted to provide assessments for other geothermal sites.

1 Introduction

An understanding of the strength and elastic modulus of rock within a geothermal reservoir is an important input in models that guide reservoir prospection, stimulation, and optimisation strategies. Laboratory experiments designed to measure these parameters are typically performed on samples with dimensions shorter than the meso- or macrofracture length scale. As a result, laboratory data gathered on nominally intact rock cannot be directly applied to large-scale geotechnical practices. Although upscaling laboratory values to the reservoir- or borehole-scale is non-trivial, widely used empirical geotechnical tools exist to bridge this length scale discrepancy. Two equations from the geotechnical toolbox, which provide estimates for rock mass strength and rock mass elastic modulus, respectively, are the generalised Hoek-Brown failure criterion (Hoek et al., 2002) and the Hoek-Diederichs equation (Hoek and Diederichs, 2006). Both of these approaches take an assessment of the rock mass structure (e.g., fracture density) and the surface condition of the fractures (e.g., smooth/rough, the pervasiveness of weathering or alteration, the nature of the fracture infilling) into account to determine the rock mass strength and elastic modulus, which will be often less than that of the intact material.

Geothermal energy exploitation is common in the Upper Rhine Graben, a 350 km-long and 50 km-wide Cenozoic rift valley that extends from Frankfurt (Germany) down to Basel (Switzerland), due

to the presence of anomalously high thermal gradients (areas of geothermal interest typically have thermal gradients > 80 °C) attributed to hydrothermal circulation within the fractured Palaeozoic granitic basement and the overlying Permian and Triassic sedimentary rocks (e.g., Pribnow and Schellschmidt, 2000; Buchmann and Connelly, 2007; Guillou-Frottier et al., 2013; Baillieux et al., 2013; Magnenet et al., 2014; Freymark et al., 2017). A total of 15 geothermal wells have been drilled (to depths between ~1000 and ~5000 m) in the Upper Rhine Graben since the 1980s (Vidal and Genter, 2018) and notable geothermal sites include Soultz-sous-Forêts (e.g., Kappelmeyer et al., 1991; Baria et al., 1999; Gérard et al., 2006; Figure 1) and Rittershoffen (e.g., Baujard et al., 2017; Glaas et al., 2018; Figure 1) in France, Brühl (e.g., Bauer et al., 2017), Insheim, Trebur, and Bruchsal in Germany, and Riehen in Switzerland.

A recent study (Villeneuve et al., 2018) provided rock mass strengths (using the generalised Hoek-Brown failure criterion; Hoek et al., 2002) and elastic moduli (using the Hoek-Diederichs equation; Hoek and Diederichs, 2006) for the fractured Palaeozoic granitic basement from exploration well EPS-1 at the Soultz-sous-Forêts geothermal site (Figure 1) using laboratory experiments on intact material and structural data from core analyses. Our goal here, using the same approach, is to provide estimates of borehole-scale rock mass strength and elastic modulus for the lowermost overlying Permian and Triassic sedimentary rocks sampled from exploration well EPS-1 (located about 1 km southwest of Soultz-sous-Forêts; Figure 1), from a depth of 1008 to 1414 m (i.e. the Buntsandstein lithostratigraphic unit). The reasons for choosing Soultz-sous-Forêts as a case study are twofold. First, the Buntsandstein was continuously cored at exploration well EPS-1 (to a core diameter of 78 mm), providing the samples required for laboratory testing (uniaxial and triaxial compression experiments). Second, there exists a wealth of structural data (fracture density and fracture fill, for example) for the borehole at EPS-1, providing the data required for the assessment of rock mass structure. Since the Buntsandstein is known to be laterally extensive (Aichholzer et al., 2016; Vidal and Genter, 2018), the results of this study can not only be used to help optimise current geothermal sites in the Upper Rhine Graben, but also to help guide and optimise future geothermal sites currently in development, such as those at Illkirch and Vendenheim (both in Alsace, France). One of the principal motivations for this study is that recent (e.g., Rittershoffen; Baujard et al., 2017; Figure 1) and future geothermal exploitation in the Upper Rhine

Graben has and will target the interface between the granitic basement and the overlying Permian and Triassic sedimentary rocks.

Providing estimates of rock mass strength and elastic modulus for the Buntsandstein is complicated for two principal reasons. First, the petrophysical variability of the Buntsandstein (e.g., Vernoux et al., 1995; Aichholzer et al., 2016; Heap et al., 2017) demands that the intact rock properties (strength and elastic modulus) are characterised for materials sampled from a number of different depths. Although the assumption of mechanical homogeneity (i.e. similar intact strength and elastic modulus at different depths) was justified when providing rock mass properties of the porphyritic granite (monzogranite) from EPS-1 from a depth of 1414 to 2200 m (Villeneuve et al., 2018), the mechanical properties of the Buntsandstein vary considerably due to the variability in porosity and microstructural attributes such as pore size and grain size (Vernoux et al., 2005; Haffen et al., 2013; Griffiths et al., 2016; Heap et al., 2017; Kushnir et al., 2018a), parameters known to greatly influence the strength and stiffness of rocks, including sandstone (e.g., Palchik et al., 1999; Chang et al., 2006; Baud et al., 2014). Here, therefore, we perform systematic laboratory measurements on material sampled at regular depth intervals (from 1008 to 1414 m) from the EPS-1 core at the Soultz-sous-Forêts geothermal site. Second, experimental studies have shown that clay plays an important role in the observed weakening of sandstone in the presence of water (e.g., Rutter and Mainprice, 1978; Hawkins and McConnell, 1992; Baud et al., 2000; Demarco et al., 2007). For example, Hawkins and McConnell (1992) found that the uniaxial compressive strength (UCS) of sandstone was reduced by 78% for clay-rich sandstones and by only 8% for siliceous sandstones in the presence of water. The variable, and sometimes high, clay contents of the Buntsandstein sandstones (e.g., Heap et al., 2017) thus calls into question the use of laboratory strength and elastic moduli data determined for dry rocks typically used in geotechnical rock mass assessments. Therefore, we here perform dry and wet laboratory deformation measurements to provide estimations of the dry and wet rock mass strength and elastic modulus for the Buntsandstein unit at the Soultz-sous-Forêts geothermal site.

2 Methods and materials

2.1 Intact failure criteria

110 The strength of intact rock, including sandstone, in the brittle regime increases with increasing
111 confining pressure or depth (e.g., Wong et al., 1997; Baud et al., 2000; Bésuelle et al., 2003). The Hoek-
112 Brown failure criterion for intact rock is an empirical failure criterion that provides strength estimates
113 for intact rock at depth using the uniaxial compressive strength, C_o, (i.e., the strength of the rock at
114 ambient pressure) and a constant, m_i:
115
116 $$\sigma_1' = \sigma_3' + C_o\left(m_i\frac{\sigma_3'}{C_o} + 1\right)^{0.5} \quad (1)$$
117
118 where σ_1' and σ_3' are the effective maximum and minimum principal stresses, respectively. The unitless
119 constant m_i describes the shape of the failure envelope on a graph of σ_1' as a function of σ_3', and is
120 therefore related to the microstructural and mineralogical attributes of the rock (mineral content, grain
121 size, grain shape, pore size, and pore shape, amongst many others) (Eberhardt, 2012). The most reliable
122 method to determine m_i is to run a series of triaxial deformation experiments on the rock of interest
123 (Hoek and Brown, 1980); however values of m_i are often estimated using charts that offer values for
124 common lithologies (e.g., Hoek and Brown, 1997).
125 In this study, C_o is determined for samples of Buntsandstein sandstone taken from regular depth
126 intervals (every 40 to 50 m) from the continuous core available at the EPS-1 exploration well (Figure
127 1). Values of empirical constant m_i are often taken from tables of "standard" values for common
128 lithologies; the recommended value of m_i for sandstone is 19 (Hoek and Brown, 1997). However, in
129 our study, we chose instead to perform a suite of triaxial experiments on samples from one of the
130 sampled depth intervals in order to better constrain m_i for the Buntsandstein (see Section 2.6). Uniaxial
131 experiments were performed under both dry and wet conditions to provide the dry intact uniaxial
132 strength, C_{o_d}, and the wet intact uniaxial strength, C_{o_w} (see Section 2.5). Similarly, wet and dry triaxial
133 experiments provide estimates for m_i under dry conditions, m_{i_d}, and under wet conditions, m_{i_w} (see
134 Section 2.6). Therefore, Equation (1) can be modified to provide the intact rock strength with depth for
135 dry (Equation 2) and wet rock (Equation 3), respectively:
136

$$\sigma_1' = \sigma_3' + C_{o\_d}\left(m_{i\_d}\frac{\sigma_3'}{C_o} + 1\right)^{0.5} \quad (2)$$

$$\sigma_1' = \sigma_3' + C_{o\_w}\left(m_{i\_w}\frac{\sigma_3'}{C_o} + 1\right)^{0.5} \quad (3)$$

2.2 Rock mass strength failure criteria

Rock mass strength can be determined using the generalised Hoek-Brown failure criterion:

$$\sigma_1' = \sigma_3' + C_o\left(m_b\frac{\sigma_3'}{C_o} + s\right)^{a} \quad (4)$$

where m_b, s, and a are unitless fitting parameters for a fractured rock mass and are defined as follows (Hoek et al., 2002):

$$m_b = m_i\, e^{\left(\frac{GSI-100}{28-14D}\right)} \quad (5)$$

$$s = e^{\left(\frac{GSI-100}{9-3D}\right)} \quad (6)$$

$$a = \frac{1}{2} + \frac{1}{6}\left(e^{-\frac{GSI}{15}} + e^{\frac{-20}{3}}\right) \quad (7)$$

where D is a unitless disturbance factor related to blasting damage in large excavations (since well drilling does not use explosives, D = 0 in our case study; we provide the full equation here for completeness) and GSI is the Geological Strength Index, a unitless value that describes the rock mass characteristics (Marinos et al., 2005). Values of GSI range from 0 to 100, where high values indicate intact or massive rock masses with fresh surfaces and low values indicate blocky/disintegrated/laminated rock masses with highly weathered surfaces and clay coatings or fillings (Marinos et al., 2005). GSI is typically obtained from rock outcrop exposures, but for this study values of GSI were determined using structural data collected on the EPS-1 core material (see Section 2.7), as

described in Villeneuve et al. (2018). Equation (4) can be recast to provide the rock mass strength with depth for dry (Equation 8) and wet rock (Equation 9), respectively:

$$\sigma_1' = \sigma_3' + C_{o\_d}\left(m_{b\_d}\frac{\sigma_3'}{C_{o\_d}} + s\right)^a \quad (8)$$

$$\sigma_1' = \sigma_3' + C_{o\_w}\left(m_{b\_w}\frac{\sigma_3'}{C_{o\_w}} + s\right)^a \quad (9)$$

where m_{b_d} and m_{b_w} are given as, respectively:

$$m_{b\_d} = m_{i\_d}\, e^{\left(\frac{GSI-100}{28-14D}\right)} \quad (10)$$

$$m_{b\_w} = m_{i\_w}\, e^{\left(\frac{GSI-100}{28-14D}\right)} \quad (11)$$

2.3 Intact and rock mass elastic modulus

The elastic modulus of intact rock, E_i, can be determined from the elastic portion of the stress-strain curve of a rock deforming in compression. The rock mass elastic modulus, E_{rm}, can be determined using the Hoek-Diederichs equation (Hoek and Diederichs, 2006):

$$E_{rm} = E_i\left(0.02 + \frac{1-\frac{D}{2}}{1+e^{\left((60+15D-GSI)/11\right)}}\right) \quad (12)$$

As for the rock strength equations in Section 2.2, the disturbance factor D is equal to zero for our application. As mentioned in Section 2.2, values of GSI were determined using structural data collected on the EPS-1 core material (see Section 2.7). Equation (12) can be modified to provide values for the elastic modulus of a dry (Equation 13) and wet rock mass (Equation 14), respectively:

185 $$E_{rm\_d} = E_{i\_d}\left(0.02 + \frac{1-\frac{D}{2}}{1+e^{\left((60+15D-GSI)/11\right)}}\right) \quad (13)$$

186

187 $$E_{rm\_w} = E_{i\_w}\left(0.02 + \frac{1-\frac{D}{2}}{1+e^{\left((60+15D-GSI)/11\right)}}\right) \quad (14)$$

188

189 where E_{i_d} and E_{i_w} are the intact elastic moduli of dry and wet rock, respectively.

190

191 2.4 Experimental materials and sample preparation

192 The Buntsandstein lithostratigraphic unit was sampled at regular (~40-50 m) depth intervals
193 (between 1008 to 1414 m; Figure 1b) from the EPS-1 exploration well from the Soultz-sous-Forêts
194 geothermal site (Figures 1 and 2). This Permian and Triassic sedimentary unit (described in, for example,
195 Vernoux et al., 2005; Haffen et al., 2013; Vidal et al., 2015; Aichholzer et al., 2016; Griffiths et al.,
196 2016; Heap et al., 2017; Kushnir et al., 2018a) directly overlies the fractured Palaeozoic granitic
197 reservoir (described in, for example, Genter and Traineau, 1996; Genter et al., 1997; Sausse et al., 2006;
198 Dezayes et al., 2010; Genter et al., 2010). We collected 1 m-long pieces of the 78 mm-diameter core at
199 each of the sampled depths. In total, twelve depths were sampled (one sandstone from the *Voltzia* unit,
200 one from the *Couches Intermédiaires* unit, three from the *Karlstal* unit, two from the *Rehberg* unit, two
201 from the *Trifels* unit, two from the *Annweiler* unit, and one from the *Anté-Annweiler* unit; Figure 1b).
202 Four or five cylindrical samples, 20, 18.75, or 12 mm in diameter (depending on the strength of the
203 sandstone), were cored from each of the twelve cores collected and precision-ground to a nominal length
204 of 40, 37.5, or 24 mm, respectively. These samples were cored so that their axes were parallel to the
205 EPS-1 borehole (i.e. perpendicular to bedding; Figure 2). We complement these borehole samples with
206 samples prepared from blocks (all from the Buntsandstein) acquired from local quarries (from Rothbach,
207 Adamswiller, and Bust, all in France; see Figure 1c for quarry locations). Samples from the quarry
208 blocks were cored perpendicular to bedding to a diameter of 20 mm and precision-ground to a nominal

length of 40 mm. All of the samples were washed using tapwater and then dried in a vacuum oven at 40 °C for at least 48 hours.

The twelve samples collected from exploration well EPS-1 are feldspathic (>10 wt.% feldspar) or quartz-rich (<10 wt.% feldspar) sandstones that contain variable amounts of pore-filling clay (muscovite/illite–smectite) (from 2 to 13.1 wt.%) (Figure 3; Table 1; Heap et al., 2017). Most of the sandstones are homogeneous at the sample scale, although a few (in particular samples 299, 497, and 540) contain obvious bedding-parallel laminations (Figure 2). The average grain diameter of these samples varies from 142 to 424 μm (Figure 3; Table 2; Heap et al., 2017). The microstructural and textural features of these samples are summarised in Table 2, and are described at length in Heap et al. (2017). The three quarry rocks are all feldspathic sandstones (Table 1). The sandstones from Bust and Adamswiller do not contain any obvious laminations/bedding, although the Adamswiller sandstone is known to exhibit a mechanical anisotropy (Baud et al., 2005). Rothbach sandstone, a rock that also shows significant mechanical anisotropy (Louis et al., 2009), however, contains alternating layers that show differences in grain size and porosity (Louis et al., 2005).

Before the samples were deformed, their connected porosity was determined using the connected (skeletal) volume measured by a helium pycnometer (Micromeritics AccuPyc II 1340) and the bulk volume calculated using the sample dimensions.

2.5 Determining C_o (intact uniaxial compressive strength) and E_i (intact elastic modulus)

The prepared cylindrical samples were deformed uniaxially at a strain rate of 1.0×10^{-6} s^{-1} until macroscopic failure. Half of the samples were deformed "dry" (dried at 40 °C in a vacuum-oven for at least 48 hours prior to deformation) and half were deformed "wet" (vacuum-saturated in deionised water and deformed in a water bath) (see Heap at al. (2014) for a schematic of the experimental device). A lubricating wax was applied to the end-faces of the dry samples to avoid problems associated with the friction between the sample and the pistons. We chose to deform the samples at a relatively low strain rate of 1.0×10^{-6} s^{-1} to ensure drainage in the low-porosity, low-permeability samples deformed under saturated conditions. During deformation, axial displacement and axial load were measured using a linear variable differential transducer (LVDT) and a load cell, respectively. These measurements were

converted to axial strain and axial stress using the sample dimensions. C_{o_d} and C_{o_w} were taken as the peak stress obtained in these uniaxial compressive strength tests under dry and wet conditions, respectively. Values of E_{i_d} and E_{i_w} were determined using the slope of the linear elastic portion of the dry and wet uniaxial stress-strain curves, respectively (Ulusay and Hudson, 2007).

2.6 Determining m_i

The unitless parameter m_i describes the shape of the failure envelope in a graph of σ_1' as a function of σ_3' (i.e. the principal stress space). We determined m_i using triaxial experiments conducted on dry and wet cylindrical cores (20 mm in diameter and 40 mm in length) prepared from the core sampled from a depth of 1239 m (from the *Rehberg* unit; porosity 0.18). Constant strain rate (1.0×10^{-6} s^{-1}) triaxial experiments were performed at constant effective pressures (defined here as the confining pressure minus the pore fluid pressure) of 2.5, 5, 7.5, 10, and 15 MPa. Samples deformed under dry conditions were therefore deformed at constant confining pressures of 2.5, 5, 7.5, 10, and 15 MPa (pore pressure = 0 MPa). A lubricating wax was applied to the end-faces of the dry samples to avoid problems associated with the friction between the sample and the pistons. Samples deformed under wet conditions were deformed using a constant pore fluid (deionised water) pressure of 10 MPa, and confining pressures of 12.5, 15, 17.5, 20, and 25 MPa. The confining and pore pressures were maintained constant during deformation using a confining and pore fluid pressure intensifier, respectively. During deformation, axial displacement and axial load were measured using an LVDT and a load cell, respectively. These measurements were converted to axial strain and axial stress using the sample dimensions. We determined m_{i_d} and m_{i_w} using the compressive strengths measured for these experiments using the data fitting function (modified cuckoo fit algorithm, basic error summation, and absolute error type) in RocData (Rocscience, 2017).

2.7 Determining the Geological Strength Index (GSI)

The GSI is a unitless value that describes the rock mass characteristics using an assessment of the rock mass structure (e.g., fracture density) and the surface condition of the fractures (e.g.,

smooth/rough, the pervasiveness of weathering or alteration, the nature and thickness of the fracture infilling) (Marinos et al., 2005). The logging data from EPS-1 in the Bundsandstein contains the type, location (depth), orientation, infilling type, and infilling thickness of all discontinuities mapped along the core. The locations (depths) were used to derive a fracture frequency. The discontinuity type, infilling type, and infilling thickness were used to assess the joint condition. The rock mass structure and surface condition were assigned broad descriptors, such as "blocky" and "poor", respectively, which were then used to determine a GSI value using a visual look-up chart (Marinos et al., 2005). Due to the available logging data and core photographs, we consider that our GSI estimates lack the subjectivity often associated with estimates of GSI.

The determination of the surface quality is relatively straightforward in this case study because of the high quality of the core logs in the Bundsandstein. Despite not having descriptions of joint roughness, we feel confident that our assessments using discontinuity type, infilling type, and infilling thickness provide a suitable basis for assessing the joint condition. For example, discontinuities identified as faults can be assumed to have smooth to slickensided surfaces, resulting in a condition assessment of fair if they have no infilling, or very poor if they have thick (> 2 mm), clayey infilling. Discontinuities identified as joints can be assumed to have rough to smooth surfaces, resulting in a condition assessment of very good if they have no infilling, or very poor if they have thick (> 2 mm), clayey infilling.

The determination of the rock mass structure requires the selection of the scale at which the rock mass assessment is conducted. For example, Villeneuve et al. (2018) assessed the rock mass strength and elastic modulus of the granite underlying the Bundsandstein at the borehole scale. These authors demonstrated that the rock mass is so densely fractured in some intervals that the intact rock parameters are not appropriate. Villeneuve et al. (2018) suggested a range of 7-10 fractures per metre as the cut-off fracture density to decide between using the intact rock failure criterion (Equation 1) and using the rock mass failure criterion (Equation 4). In the present case study we derive the rock mass parameters at the reservoir scale (tens of metres). Based on the recommendations of Schultz (1996), we use a block size to reservoir scale ratio of 5-10 as the cutoff for using rock mass strength and elastic modulus. We use fracture densities of 1 fracture per metre and 2 fractures per metre to differentiate between massive and

292 blocky, and blocky and very blocky, respectively. In accordance with the reasoning detailed in
293 Villeneuve et al. (2018), the cut-off between intact and rock mass failure criteria corresponds to
294 approximately 2 fractures per metre.
295
296 **3 Laboratory testing**
297 3.1 Uniaxial compressive strength experiments
298 Representative uniaxial stress-strain curves for the dry Buntsandstein samples are shown in
299 Figure 4a. These stress-strain curves (Figure 4a) are typical of those for brittle rock in compression (e.g.,
300 Hoek and Bieniawski, 1965; Brace et al., 1966; Scholz, 1968). The maximum axial stress obtained
301 during the experiment is the uniaxial compressive strength, C_o (as labelled for one of the dry curves in
302 Figure 4a). Representative uniaxial stress-strain curves for a dry and wet sample of sample 100 are
303 shown in Figure 4b. These curves show that the uniaxial compressive strength is lower when the sample
304 is wet. In the example shown in Figure 4b, the dry strength, C_{o_d}, was 150.8 MPa and the wet strength,
305 C_{o_w}, was 89.9 MPa. These representative curves also show that the slope of the stress-strain curve in
306 the elastic region (i.e. the elastic modulus) and the axial strain at macroscopic failure are lower when
307 the sample is wet (Figure 4b).
308 Dry (white circles) and wet (blue squares) uniaxial compressive strengths (C_{o_d} and C_{o_w},
309 respectively) and elastic moduli (E_{i_d} and E_{i_w}, respectively) are plotted as a function of connected
310 porosity in Figures 5a and 5b, respectively (data available in Table 3). These data show that the strength
311 (Figure 5a) and elastic modulus (Figure 5b) of the Buntsandstein samples studied here both decrease as
312 the connected porosity is increased. For example, the dry strength and dry elastic modulus of the
313 Buntsandstein samples tested herein range from ~50 MPa and ~10 GPa, respectively, at a porosity of
314 ~0.25 up to ~250 MPa and ~40 GPa, respectively, at a porosity of ~0.04 (Figures 5a and 5b). These data
315 also show that the wet strength and wet elastic modulus of the sandstones is systematically lower than
316 the dry strength and elastic modulus across the entire tested porosity range (Figures 5a and 5b).
317 The ratios of wet to dry strength are plotted as a function of connected porosity and clay content
318 in Figures 6a and 6b, respectively. These data show that the ratio of wet to dry strength varies from

~0.55 to ~0.84 for the rocks tested herein (Figure 6). Figure 6a shows that the observed water-weakening does not appear to depend on the connected porosity. However, although there is some scatter in the data, there is a trend of increasing water-weakening as clay content is increased (Figure 6b). Indeed, the sample that contains the most clay (13.1 wt.%; sample 540) has the lowest ratio of wet to dry strength, and the sample containing the least clay (1.8 wt.%; Rothbach sandstone) has the highest ratio of wet to dry strength (Figure 6b). The ratios of wet to dry elastic modulus are plotted as a function of connected porosity and clay content in Figures 7a and 7b, respectively. These data show that the ratio of wet to dry elastic modulus varies from ~0.74 to ~1.00 for the rocks tested herein (Figure 7). The ratio of wet to dry elastic modulus does not appear to depend on either connected porosity (Figure 7a) or clay content (Figure 7b).

3.2 Triaxial compressive strength experiments

The stress-strain curves for the dry and wet triaxial experiments (on samples from sample 347) are shown in Figures 8a and 8b, respectively (experiments unique to this study). The sandstone is brittle over the tested pressure range and failure (marked by a stress drop in the stress-strain data; Figure 8) was manifest as a through-going shear fracture. These data show that the dry (Figure 8a) and wet (Figure 8b) strength increases as the effective pressure is increased, in accordance with many experimental studies on sandstones in the brittle field (e.g., Wong et al., 1997; Baud et al., 2000; Bésuelle et al., 2003). For example, the dry strength was increased from ~58 MPa at an effective pressure of 0 MPa to ~141 MPa at an effective pressure of 15 MPa (Figure 8a) (data available in Table 4). Our triaxial experiments also show that sample 347 is weaker when wet over the entire tested range of effective pressure (i.e. up to 15 MPa) (Figure 8).

The triaxial data plotted in principal stress space ($\square_1$ as a function of $\square_3$; Figure 9) show that the failure envelope for the wet samples (blue symbols in Figure 9) is lower than the failure envelope for the dry samples (white symbols in Figure 9). The fits to these data were provided by the Modified Cuckoo data fitting algorithm using basic (vertical) error summation, and relative (divided by the y-value of the curve fit) error type) in RocData (Rocscience, 2017). These fits provide values of 19 (relative residuals 0.008) and 23 (relative residuals 0.012) for m_{i_d} and m_{i_w}, respectively. We note that

347 the value for dry sandstone is within the range of m_i values typically associated with sandstone (17 ± 4,
348 as given in Hoek (2007)), whereas the value for wet sandstone is slightly higher than this range.
349
350 3.3 Geological Strength Index (GSI)
351 The rock mass descriptions, based on fracture frequency, infilling type, and infilling thickness
352 are summarised in Table 5, along with their associated rock mass descriptions at the reservoir scale.
353 Figure 10 shows how the look-up chart from Marinos et al. (2005) was used to assess the GSI for two
354 example intervals. For the depth interval 1365-1381 m the fracture density is 2.1 fractures per metre,
355 and is therefore assessed as a "very blocky" (see Figure 10) rock mass structure. The fractures are infilled
356 with barite and minor calcite (both hard minerals that tend to seal fractures) with an infilling thickness
357 averaging 2 mm. The surface condition of the fractures is therefore assessed as "good" (see Figure 10)
358 because barite and calcite are precipitated mineral infillings and will therefore contribute cohesive and
359 frictional strength to the fracture. The combination of the two assessments results in a GSI range of 45-
360 60. Since our analysis requires a single value of GSI, we use GSI = 55 for this interval (1365-1381 m)
361 (Table 5). Similarly, the depth interval 1012-1020 m has been assessed a "very blocky" (see Figure 10)
362 structure. Because of the presence of four faults within an 8 m thick interval, and an infilling thickness
363 averaging 9 mm, the surface condition is assessed as "poor" (see Figure 10). The combination results in
364 a range of GSI of 25-40. Again, since our analysis requires a single value of GSI, we use GSI = 35 for
365 this interval (1012-1020 m) (Table 5).
366 The majority of the rock mass in the Bundsandstein has a GSI of 100 (Table 5) because of its
367 low fracture density (< 2 fractures per metre), with the resulting assessment of "massive" for the rock
368 structure and the use of the intact Hoek-Brown failure criterion (Equation 1) to determine rock strength
369 over these intervals. The intervals with GSI less than 100, of which there are five, are associated with
370 highly fractured zones (e.g., the interval between depths 1151 and 1156 m has a fracture density of 2
371 discontinuities per metre) (Table 5). The five zones that are characterised by low values of GSI are
372 located at depths of ~1012-1020, ~1151-1156, ~1205-1216, ~1347-1350, and ~1365-1381 m (Table 5).
373 The zones with the lowest GSI (GSI = 35) are associated with highly fractured zones that contain
374 fractures with a very thick average infilling (e.g., the interval between depths 1205 and 1216 m has an

375 average infilling thickness of 11 mm; Table 5). The three zones with the lowest GSI (Table 5) were
376 previously identified as the three main fractured zones within the EPS-1 core (Vernoux et al., 2005).
377
378 **4 Reservoir-scale strength and elastic modulus for the Buntsandstein**
379 The dry and wet intact and rock mass strength and elastic modulus, calculated using the reservoir
380 scale GSI and Equations 1, 2, 3, 8, and 9 (for the strength) and Equations 13 and 14 (for the elastic
381 modulus) are given in Table 5. The fracture density with depth (Figure 11a) is plotted alongside the dry
382 and wet strength and elastic modulus in Figures 11b and 11c, respectively. Figures 11b and 11c clearly
383 show the five zones for which the rock mass strength and rock mass elastic modulus is applicable (at
384 depths of ~1012-1020, ~1151-1156, ~1205-1216, ~1347-1350, and ~1365-1381 m; indicated by the
385 black arrows in Figure 11), as opposed to those where the intact values of either property are appropriate.
386 These zones are characterised by low values of strength (Figure 11b) and elastic modulus (Figure 11c).
387 Apart from these five zones, the strength and elastic modulus of the rock mass is given by the intact
388 strength and the intact elastic modulus (GSI = 100; Table 5). Excluding the rock at the interface between
389 the granite and the sedimentary rocks (the *Anté-Annweiler*), which has relatively high values of strength
390 and elastic modulus, the overall strength (Figure 11b) and elastic modulus (Figure 11c) of the
391 Buntsandstein appears to decrease with depth; this is especially true for the elastic modulus (Figure 11c).
392 We also note that, in the five zones where the strength and elastic modulus are described by the
393 rock mass strength and elastic modulus, respectively, there is essentially no difference between the dry
394 and wet values (Figures 11b and 11c). In these zones, the strength and elastic modulus of the rock mass
395 very much depends on the fractures present within the rock mass, rather than the condition (wet or dry)
396 of the rock mass. However, in the depths characterised by the intact strength and elastic modulus, a large
397 difference can be observed between the wet and dry values (Figures 11b and 11c).
398
399 **5 Discussion**
400 5.1 Water-weakening in sandstones
401 Water-weakening in rocks can be the result of both mechanical and chemical processes.
402 Mechanically, pressurised pore fluids typically weaken and embrittle rocks (e.g. Paterson and Wong,

403 2005). Chemically, rock can be weakened by subcritical crack growth processes (e.g., Atkinson, 1984)
404 and the reduction of surface free energy (e.g., Parks, 1984). The mechanical effect can be expressed in
405 terms of the effective pressure law, where the effective pressure equals the confining pressure minus the
406 pore fluid pressure multiplied by a poroelastic constant. The study of Baud et al. (2015) shows that this
407 poroelastic constant is very close to unity for porous sandstone. As a result, we do not consider herein
408 the mechanical influence of pore fluids on the strength of our sandstone samples.

409 Our deformation experiments have shown that sandstone is weaker in the presence of water
410 (Figures 4, 5, 6, 7, and 8), in accordance with many published studies (e.g., Rutter and Mainprice, 1978;
411 Bell, 1978; Hadizadeh and Law, 1991; Dyke and Dobereiner, 1991; Hawkins and McConnell, 1992;
412 Kasim and Shakoor, 1996; Zang et al., 1996; Bell and Culshaw, 1998; Baud et al., 2000; Cuss et al.,
413 2003; Lin et al., 2005; Vásárhelyi and Ván, 2006; Demarco et al., 2007; Shakoor and Barefield, 2009;
414 Nespereia et al., 2010; Siedel, 2010; Wasantha and Ranjith, 2014). A handful of these studies highlight
415 that the observed water-weakening in sandstones is related to their clay content. For example, Hawkins
416 and McConnell (1992) found that the uniaxial compressive strength (UCS) of sandstone was reduced
417 by 78% for clay-rich sandstones and by only 8% for siliceous sandstones in the presence of water.
418 Although our data suggest that the water-weakening in sandstone does not depend on connected porosity
419 (Figure 6a), they do highlight that water-weakening may increase as clay content is increased (Figure
420 6b). To better understand the role of connected porosity and clay content on water-weakening in
421 sandstone, we plot ratios of wet to dry strength from numerous studies (data available in Table 6)
422 alongside our new data (Table 3) as a function of porosity and clay content in Figures 12a and 12b,
423 respectively. Figure 12a shows that there is no discernible trend between water-weakening in sandstone
424 and porosity. However, Figure 12b shows that, although there is some scatter in the data, water-
425 weakening increases as clay content is increased. Indeed, the sample containing the highest clay content
426 (~70 %) has the lowest ratio of wet to dry strength (Figure 12b).

427 To explore the reason for the reduction in strength in the presence of water we use the
428 micromechanical model of Sammis and Ashby (1986). This model, based on the classic work of
429 Griffiths, has been previously used to describe the brittle failure of porous sandstones (e.g., Baud et al.,
430 2014). The micromechanical model of Sammis and Ashby (1986) is an inclusion model comprising a

two-dimensional elastic medium populated by circular holes of uniform radius, r. As the stress on the medium increases, cracks nucleate and propagate from the circular holes (parallel to the direction of the applied stress) when the stress intensity at the tip of a small crack on the circular surface reaches a critical value (K_{IC}, the fracture toughness). The cracks interact once they are long enough, thus increasing the local tensile stress intensity. Eventually, the cracks coalesce and conspire to induce the macroscopic failure of the elastic medium. In the case of uniaxial compression, Zhu et al. (2010) provide an analytical approximation of Sammis and Ashby's (1986) model to estimate UCS as a function of porosity, ϕ:

$$C_0 = \frac{1.325}{\phi^{0.414}} \frac{K_{IC}}{\sqrt{\pi r}} \quad (15)$$

Assuming that Equation (15) can capture the behaviour of the sandstones of Table 6, there are three variables that influence uniaxial compressive strength: the porosity, ϕ, the fracture toughness, K_{IC}, and the pore radius, r. If we assume that the porosity and pore radius are the same for a given sandstone then, according to Equation (15), the observed water-weakening (Figure 12) must be due to a decrease in K_{IC}. Figure 13 shows strength as a function of porosity using Equation (15) for a fixed pore radius (125 μm) and different values of K_{IC} (K_{IC} = 0.1, 0.3, 0.5, and 0.8 MPa m$^{-1/2}$) alongside the dry (white circles) and wet (blue squares) data for the compiled sandstones. These modelled curves aptly demonstrate that decreasing the K_{IC} at a given porosity and pore size lowers the strength (Figure 13). The reduction in uniaxial compressive strength observed in wet rocks has been attributed to a reduction in fracture surface free energy due to the adsorption of water on the fracture surface (e.g., Parks, 1984; Baud et al., 2000). We conclude here, in line with the conclusions of Baud et al. (2000), that a lower fracture surface free energy in the presence of water reduces K_{IC} and therefore strength. Additionally, we highlight that water adsorption on clay minerals is extremely efficient due to their large surface areas. To emphasise, the specific surface areas of samples 157 (clay content = 2 wt.%) and 540 (clay content = 13.1 wt.%) are 204 and 6170 m^2/kg, respectively (Heap et al., 2017; Tables 1 and 2). Therefore, a higher clay content should ensure that more water is adsorbed on the surface of the fracture, perhaps

458 explaining the correlation between clay content and water-weakening (Figure 12b). The scatter in the
459 data of Figure 12b suggests that clay content does not govern water-weakening in sandstones alone. One
460 factor likely to play a key role is whether the clays are pore-coating or pore-filling, or whether the clays
461 are present within the rock matrix. For water adsorption on clay minerals to influence the fracture surface
462 free energy, the clays must be present within the material through which the fracture propagates (i.e. the
463 matrix). By contrast, clay present within pores may not exert a significant influence on the water-
464 weakening process.

465 We further highlight that the micromechanics of low-porosity rocks is often described using the
466 wing-crack model of Ashby and Sammis (1990), although we note that no or few microcracks were
467 found in the intact microstructure of the studied materials (Figure 3). If the wing-crack model was
468 considered appropriate for the low-porosity materials studied herein, then there is an additional
469 micromechanical parameter—the coefficient of friction—could also be influenced by the presence of
470 water.

471

472 5.2 Implications for geothermal energy exploitation

473 We have provided estimates of the rock mass strength (Figure 11b) and elastic modulus (Figure
474 11c) for the Bundsandstein sedimentary sequence (from the Soultz-sous-Forêts geothermal site) that
475 directly overlies the fractured granitic basement used throughout the Upper Rhine Graben as a
476 geothermal resource. One of the main motivations for this study is that recent (e.g., Rittershoffen;
477 Baujard et al., 2017) and future geothermal exploitation in the Upper Rhine Graben has and will target
478 rock at or close to this interface. Since the Buntsandstein is known to be a laterally extensive unit (e.g.
479 Aichholzer et al., 2016; Vidal and Genter, 2018), these new reservoir-scale strength and elastic modulus
480 estimates could assist prospection, stimulation, and optimisation strategies (for instance, the
481 Buntsandstein was stimulated at the Rittershoffen site in 2013; Vidal et al., 2016; Baujard et al., 2017)
482 at geothermal sites within the Upper Rhine Graben. We can combine our strength and elastic modulus
483 estimates for the Buntsandstein with those for the granite reservoir provided in Villeneuve et al. (2018)
484 to give strength (Figure 14b) and elastic modulus (Figure 15b) estimates for the EPS-1 borehole from a
485 depth of ~1000 to ~2200 m. These data highlight, for example, that the rock mass strength of the granitic

reservoir can be lower than that for the Buntsandstein, due to the high fracture density of the granite (Figure 14).

However, since the rock mass strength and elastic modulus estimations (Figures 11b, 11c, 14b, and 15b) are very much dependent on the fracture density (and their surface condition), the estimations provided herein may not be directly applicable to the Buntsandstein sedimentary sequence found at other geothermal sites, which will likely be characterised by different fracture densities and intersect regional scale faults at different depths. For example, the Buntsandstein is much deeper at the Rittershoffen site (from ~1800 to ~2200 m; Aichholzer et al., 2016) than at Soultz-sous-Forêts and major fracture zones are found at depths of ~1975, ~1986, and ~2140 m (Vidal et al., 2017). Further, the extent of fracture infilling will also be spatially variable. For instance, Vidal et al. (2015) note that the extent of the fracture sealing can differ in the same fractured zone at different wells (e.g., GPK-2, GPK-3, and GPK-4, which are separated by no more than 1.5 km) at Soultz-sous-Forêts. We further note that the sedimentary units overlying the granitic reservoir can be appreciably different from those at the Soultz-sous-Forêts site at a distance of several tens of kilometres (Kushnir et al., 2018b). However, we highlight that our laboratory data can be re-used to provide upscaled strength and elastic modulus profiles for other sites, using the methods outlined herein, as long as site-specific rock mass descriptions are performed. We highlight that direct core data will provide a more complete characterisation of the fracture network than borehole imaging tools (Genter et al., 1997). A recent study by Bauer et al. (2017) also highlights that, when core materials are not available, care should be taken when selecting outcrop analogues for geothermal reservoir rock.

Our laboratory data have shown that the Buntsandstein sandstones are weaker when wet (Figure 5). In zones characterised by the intact rock strength and elastic modulus (i.e. all zones except the five highly fractured zones) (Figures 11b and 11c), the reservoir-scale strength and the elastic modulus are lower when the rock is wet. Differences between the dry and wet strength and elastic modulus within the five fractured zones are small: the strength and elastic modulus in these zones is primarily dictated by the rock mass structure (fractures) (Figures 11b and 11c). Since the pore space of rocks within a geothermal reservoir will be saturated with liquid water/brine in-situ, our measurements and analysis therefore highlight the importance of performing wet deformation experiments to provide upscaled

514 strength and elastic modulus assessments for geothermal applications. Indeed, not only are the wet and
515 dry strengths and elastic moduli different (Figure 5), but we also measured a difference between the dry
516 and wet m_i term (Figure 9). We recommend that future studies that adopt this technique also perform
517 wet deformation experiments, particularly because water-weakening has been reported in a wide range
518 of rock types (e.g., sandstone: Hawkins and McConnell, 1992, tuff: Zhu et al., 2011; Heap et al., 2018,
519 basalt: Zhu et al., 2016, carbonates: Baud et al., 2016).

520 Although we performed wet deformation measurements to provide more accurate strength and
521 elastic modulus assessments, we highlight that our experiments were performed at room temperature
522 and used deionised water. First, the temperature of the Buntsandstein rocks at Soultz-sous-Forêts, for
523 example, is between 120 and 140 °C (e.g., Genter et al., 2010). The intact strength and stiffness of
524 sandstone measured in the laboratory may be different at high-temperature, although there is a paucity
525 of data. For example, Ranjith et al. (2012) found that the uniaxial compressive strength and stiffness of
526 Hawkesbury sandstone (containing 20% clay) increased from 36.5 to 42.5 MPa and from 2.8 to 3.3 GPa,
527 respectively, as the testing temperature was increased from 25 to 200 °C. Rao et al. (2007) also observed
528 an increase in uniaxial compressive strength and stiffness for sandstone as temperature was increased
529 from 25 to 150 °C. Therefore, based on these few data, it would appear that the rock mass strength and
530 elastic modulus assessments provided herein (measured at room temperature) may underestimate the
531 strength and elastic modulus of the rock in-situ. However, firm conclusions cannot be drawn without
532 further experimental investigations. For example, Heap et al. (2009a) showed that the compressive
533 strength of three sandstones under triaxial testing conditions (an effective pressure of 30 MPa) was
534 slightly lower at 75 °C than at room temperature. At present it is unclear as to the influence of, for
535 example, mineral content, porosity, and grain size on the compressive strength of sandstone at high-
536 temperature. Second, the rocks within the reservoir are saturated with hydrothermal brines with a pH
537 between 5.2 and 5.5 (e.g., Scheiber et al., 2002). A lower pH should reduce the fracture surface free
538 energy (e.g., Parks, 1984) and therefore reduce intact strength. Indeed, Singh et al. (1999) measured a
539 reduction in uniaxial compressive strength in sandstone from ~65 to ~40 MPa as the pH was reduced
540 from 7 to 2. The uniaxial compressive strength of sandstone samples was also found to decrease with
541 increasing salinity (Shukla et al., 2013; Rathanweera et al., 2014). However, recent triaxial experiments

showed that the triaxial compressive strength of sandstone increased with increasing NaCl concentration (Huang et al., 2018). It is therefore difficult to draw firm conclusions as to the influence of the pore fluid composition and pH on the strength and stiffness of sandstone without further laboratory testing.

We highlight that the reservoir-scale strength and elastic modulus estimates provided here are representative of the short-term strength. These rock properties, and empirical term m_i, were all determined at a laboratory strain rate of 1×10^{-6} s^{-1}. Although this strain rate is an order of magnitude lower than typically used in laboratory testing, we highlight that the strength of rock, including sandstone, decreases as strain rate is decreased due to time-dependent subcritical crack growth processes (Atkinson, 1984; Brantut et al., 2013). There are many experimental studies on time-dependent deformation in sandstone (e.g., Ngwenya et al., 2001; Baud and Meredith, 1997; Heap et al., 2009a; 2009b; Yang and Jiang, 2010; Brantut et al., 2014; Tang et al., 2018). For example, Heap et al. (2009b) showed that sandstone fails at 80% of its short-term failure stress in about 60 hours. Further, and pertinent to the geothermal reservoir case study, the deformation rate during a brittle creep test can increase by up to three orders of magnitude as the temperature is increased from 20 to 75 °C (Heap et al., 2009a). Based on the data provided in these studies, the long-term strength of the Buntsandstein sedimentary sequence may be lower than the short-term strength estimates provided herein.

5 Concluding remarks

Recent geothermal exploitation in the Upper Rhine Graben has targeted the interface between the fractured granitic basement and the overlying Permian and Triassic sedimentary rocks (the Buntsandstein), and geothermal projects being developed in the region will continue to do so. Our study provides wet and dry strength and elastic modulus estimates for the Buntsandstein sedimentary sequence (from 1008 to 1414 m) at the Soultz-sous-Forêts geothermal site in France. To provide such estimates we performed 64 uniaxial (32 dry and 32 wet) and 10 triaxial deformation experiments (5 dry and 5 wet). These data were coupled with Geological Strength Index (GSI) assessments to provide down-well wet and dry strength and elastic modulus profiles using the Hoek-Brown failure criterion and the Hoek-Diederichs equation, respectively. Our analysis finds five zones characterised by low values of GSI (zones with high fracture densities and infilling thicknesses) that have low values of rock mass strength

and elastic modulus. The zones with low fracture densities (i.e. a "massive" rock structure) are characterised by the intact rock properties (i.e. a GSI value of 100) and therefore have higher values of strength and elastic modulus. Additionally, we find that the strength and elastic modulus of these massive zones are lower when the rock is wet, highlighting the importance of performing wet deformation experiments for rock mass assessments of rock that is typically saturated with a liquid phase, such as in a geothermal reservoir. We combine these new data with those for the underlying fractured granite reservoir to produce down-well strength and elastic modulus profiles from a depth of ~1000 to ~2200 m for the Soultz-sous-Forêts geothermal site. Although this type of analysis is somewhat site specific, the methods used and data provided herein can be easily adapted to provide strength and elastic modulus estimates for other geothermal sites within the Upper Rhine Graben to assist reservoir prospection, stimulation, and optimisation strategies.

Acknowledgements

This study was funded by LABEX grant ANR-11-LABX-0050_G-EAU-THERMIE-PROFONDE (this research therefore benefited from state funding managed by the Agence National de la Recherche (ANR) as part of the "Investissements d'avenir" program) and ANR grant CANTARE (ANR-15-CE06-0014-01). We are extremely grateful to Albert Genter, who provided the fracture data from EPS-1 (we therefore also acknowledge the Bureau de Recherches Géologiques et Minières (BRGM)). We also wish to thank Chrystal Dezayes, Bertrand Renaudié, Coralie Aichholzer, and Philippe Duringer. The comments of two anonymous reviewers helped clarify certain aspects of this manuscript.

Author contributions

M.J. Heap led the project and co-wrote the manuscript with M. Villeneuve. P. Baud, M.J. Heap, and A.R.L. Kushnir chose and collected the samples from the Merkwiller core repository. M.J. Heap and A.R.L. Kushnir measured the porosity of the experimental samples. M.J. Heap performed all the uniaxial compressive strength tests. M.J. Heap, A.R.L. Kushnir, and J.I. Farquharson performed the

triaxial compressive strength tests. M. Villeneuve performed the geotechnical analyses. All authors had a hand in the preparation of the manuscript and the interpretation of the data.

599 **References**

600

601 Aichholzer C, Duringer P, Orciani S, Genter A (2016) New stratigraphic interpretation of the Soultz-
602 sous-Forêts 30-year-old geothermal wells calibrated on the recent one from Rittershoffen (Upper
603 Rhine Graben, France). Geotherm Energy 4:13.
604 Atkinson BK (1984) Subcritical crack growth in geological materials. Journal of Geophysical Research:
605 Solid Earth 89:4077-4114.
606 Baillieux P, Schill E, Edel JB, Mauri G (2013) Localization of temperature anomalies in the Upper
607 Rhine Graben: insights from geophysics and neotectonic activity. Int Geol Rev 55:1744-62.
608 Baria R, Baumgärtner J, Gérard A, Jung R, Garnish J (1999) European HDR research programme at
609 Soultz-sous-Forêts (France) 1987–1996. Geothermics 28(4):655-669.
610 Baud P, Meredith PG (1997) Damage accumulation during triaxial creep of Darley Dale sandstone from
611 pore volumometry and acoustic emission. International Journal of Rock Mechanics and Mining
612 Sciences 34:24-e1.
613 Baud P, Zhu W, Wong Tf (2000) Failure mode and weakening effect of water on sandstone. Journal of
614 Geophysical Research: Solid Earth 105(B7):16371-89.
615 Baud P, Louis L, David C, Rawling GC, Wong Tf (2005) Effects of bedding and foliation on mechanical
616 anisotropy, damage evolution and failure mode. Geological Society, London, Special
617 Publications 245:223-249.
618 Baud P, Wong Tf, Zhu W (2014) Effects of porosity and crack density on the compressive strength of
619 rocks. Int J Rock Mech Min Sci 67:202-11.
620 Baud P, Reuschlé T, Ji Y, Cheung CS, Wong Tf (2015). Mechanical compaction and strain localization
621 in Bleurswiller sandstone. Journal of Geophysical Research: Solid Earth 120(9):6501-6522.
622 Baud P, Rolland A, Heap MJ, Xu T, Nicolé M, Ferrand T, Reuschlé T, Toussaint R, Conil N (2016).
623 Impact of stylolites on the mechanical strength of limestone. Tectonophysics 690:4-20.
624 Bauer JF, Krumbholz M, Meier S, Tanner DC (2017). Predictability of properties of a fractured
625 geothermal reservoir: the opportunities and limitations of an outcrop analogue study. Geothermal
626 Energy 5(1):24.
627 Baujard C, Genter A, Dalmais E, Maurer V, Hehn R, Rosillette R, Vidal J, Schmittbuhl J (2017).
628 Hydrothermal characterization of wells GRT-1 and GRT-2 in Rittershoffen, France: Implications
629 on the understanding of natural flow systems in the Rhine graben. Geothermics 65: 255-268.
630 Bell FG (1978) Petrographical factors relating to porosity and permeability in the Fell Sandstone.
631 Quarterly Journal of Engineering Geology and Hydrogeology 11(2):113-26.
632 Bell FG, Culshaw MG (1998) Petrographic and engineering properties of sandstones from the Sneinton
633 Formation, Nottinghamshire, England. Quarterly Journal of Engineering Geology and
634 Hydrogeology 31(1):5-19.

635 Bésuelle P, Baud P, Wong, Tf (2003). Failure mode and spatial distribution of damage in Rothbach
636 sandstone in the brittle-ductile transition. *Pure and Applied Geophysics 160*(5-6):851-868.
637 Brace WF, Paulding Jr BW, Scholz CH (1966) Dilatancy in the fracture of crystalline rocks. Journal of
638 Geophysical Research 71:3939-3953.
639 Brantut N, Heap MJ, Meredith PG, Baud P (2013) Time-dependent cracking and brittle creep in crustal
640 rocks: A review. Journal of Structural Geology 52:17-43.
641 Brantut N, Heap MJ, Baud P, Meredith PG (2014) Rate-and strain-dependent brittle deformation of
642 rocks. Journal of Geophysical Research: Solid Earth 119:1818-1836.
643 Buchmann TJ, Connolly PT (2007) Contemporary kinematics of the Upper Rhine Graben: a 3D finite
644 element approach. Global and Planetary Change 58:287-309.
645 Chang C, Zoback MD, Khaksar A (2006) Empirical relations between rock strength and physical
646 properties in sedimentary rocks. J Petrol Sci Eng 51:223-37.
647 Cuss RJ, Rutter EH, Holloway RF (2003) The application of critical state soil mechanics to the
648 mechanical behaviour of porous sandstones. International Journal of Rock Mechanics and Mining
649 Sciences 40(6):847-62.
650 David C, Wong TF, Zhu W, Zhang J (1994) Laboratory measurement of compaction-induced
651 permeability change in porous rocks: Implications for the generation and maintenance of pore
652 pressure excess in the crust. Pure and Applied Geophysics 143(1-3):425-56.
653 Demarco MM, Jahns E, Rüdrich J, Oyhantcabal P, Siegesmund S (2007) The impact of partial water
654 saturation on rock strength: an experimental study on sandstone [Der Einfluss einer partiellen
655 Wassersättigung auf die mechanischen Gesteinseigenschaften: eine Fallstudie an Sandsteinen].
656 Zeitschrift der Deutschen Gesellschaft für Geowissenschaften 58(4):869-82.
657 Dezayes C, Genter A, Valley B (2010) Structure of the low permeable naturally fractured geothermal
658 reservoir at Soultz. Comptes Rendus Geoscience 342:517-530.
659 Dyke CG, Dobereiner L (1991) Evaluating the strength and deformability of sandstones. Quarterly
660 Journal of Engineering Geology and Hydrogeology 24:123-134.
661 Eberhardt E (2012) The Hoek–Brown failure criterion. In: R. Ulusay (ed.), The ISRM Suggested
662 Methods for Rock Characterization, Testing and Monitoring: 2007–2014:233-240.
663 Freymark J, Sippel J, Scheck-Wenderoth M, Bär K, Stiller M, Fritsche JG, Kracht M (2017) The deep
664 thermal field of the Upper Rhine Graben. Tectonophysics, 694, 114-129.
665 Gérard A, Genter A, Kohl T (2006) The deep EGS (Enhanced Geothermal System) project at Soultz-
666 sous-Forêts (Alsace, France). Geothermics 35:473-483.
667 Genter A, Traineau H (1996) Analysis of macroscopic fractures in granite in the HDR geothermal well
668 EPS-1, Soultz-sous-Forêts, France. Journal of Volcanology and Geothermal Research 72:121-
669 141.

Genter A, Castaing C, Dezayes C, Tenzer H, Traineau H, Villemin T (1997) Comparative analysis of direct (core) and indirect (borehole imaging tools) collection of fracture data in the Hot Dry Rock Soultz reservoir (France). Journal of Geophysical Research: Solid Earth 102:15419-15431.

Genter A, Evans K, Cuenot N, Fritsch D, Sanjuan B (2010) Contribution of the exploration of deep crystalline fractured reservoir of Soultz to the knowledge of enhanced geothermal systems (EGS). Comptes Rendus Geoscience 342:502-516.

Glaas C, Genter A, Girard JF, Patrier P, Vidal J (2018) How do the geological and geophysical signatures of permeable fractures in granitic basement evolve after long periods of natural circulation? Insights from the Rittershoffen geothermal wells (France). Geotherm Energy, 6:14.

Griffiths L, Heap MJ, Wang F, Daval D, Gilg HA, Baud P, Schmittbuhl J, Genter A (2016) Geothermal implications for fracture-filling hydrothermal precipitation. Geothermics 64:235-245.

Guillou-Frottier L, Carré C, Bourgine B, Bouchot V, Genter A (2013) Structure of hydrothermal convection in the Upper Rhine Graben as inferred from corrected temperature data and basin-scale numerical models. J Volcanol Geotherm Res 256:29-49.

Hadizadeh J, Law RD (1991) Water-weakening of sandstone and quartzite deformed at various stress and strain rates. Int J Rock Mech Min Sci Geomech Abs 28:431-439.

Haffen S, Géraud Y, Diraison M, Dezayes C (2013) Determination of fluid-flow zones in a geothermal sandstone reservoir using thermal conductivity and temperature logs. Geothermics 46:32-41.

Hawkins AB, McConnell BJ (1992) Sensitivity of sandstone strength and deformability to changes in moisture content. Quarterly Journal of Engineering Geology and Hydrogeology 25:115-30.

Heap MJ, Baud P, Meredith PG (2009a). Influence of temperature on brittle creep in sandstones. Geophysical Research Letters 36(19) https://doi.org/10.1029/2009GL039373

Heap MJ, Baud P, Meredith PG, Bell AF, Main IG (2009b). Time-dependent brittle creep in Darley Dale sandstone. Journal of Geophysical Research: Solid Earth 114(B7) https://doi.org/10.1029/2008JB006212

Heap MJ, Lavallée Y, Petrakova L, Baud P, Reuschlé T, Varley NR, Dingwell DB (2014). Microstructural controls on the physical and mechanical properties of edifice-forming andesites at Volcán de Colima, Mexico. Journal of Geophysical Research: Solid Earth 119(4):2925-2963.

Heap MJ, Kushnir ARL, Gilg HA, Wadsworth FB, Reuschlé T, Baud P (2017) Microstructural and petrophysical properties of the Permo-Triassic sandstones (Buntsandstein) from the Soultz-sous-Forêts geothermal site (France). Geotherm Energy 5(1):26.

Heap MJ, Farquharson JI, Kushnir AR, Lavallée Y, Baud P, Gilg HA, Reuschlé T (2018) The influence of water on the strength of Neapolitan Yellow Tuff, the most widely used building stone in Naples (Italy). Bulletin of Volcanology 80(6):51.

Hoek E, Bieniawski ZT (1965) Brittle fracture propagation in rock under compression. International Journal of Fracture Mechanics 1:137-155.

706 Hoek E, Brown ET (1980) Empirical Strength Criterion for Rock Masses. J Geotech Geoenviron Eng
707 106 (GT9):1013-1035.
708 Hoek E, Brown ET (1997) Practical estimates of rock mass strength. International Journal of Rock
709 Mechanics and Mining Sciences, 34(8), 1165-1186.
710 Hoek E, Carranza-Torres CT, Corkum B (2002) Hoek–Brown failure criterion—2002 edition. In:
711 Hammah R, Bawden W, Curran J, Telesnicki M (eds) Proceedings of the Fifth North American
712 Rock Mechanics Symposium (NARMS-TAC), University of Toronto Press, Toronto: 267-273.
713 Hoek E, Diederichs MS (2006) Empirical estimation of rock mass modulus. Int J Rock Mech Min Sci
714 43(2):203-215.
715 Hoek E (2007) Practical Rock Engineering. e-book: https://www.rocscience.com/learning/hoek-s-
716 corner/books.
717 Huang YH, Yang SQ, Hall MR, Zhang YC (2018) The Effects of NaCl Concentration and Confining
718 Pressure on Mechanical and Acoustic Behaviors of Brine-Saturated Sandstone. Energies
719 11(2):385.
720 Kappelmeyer O, Gérard A, Schloemer W, Ferrandes R, Rummel F, Benderitter Y (1991) European HDR
721 project at Soultz-sous-Forêts: general presentation. Geotherm Sci Tech 2(4):263-289.
722 Kasim M, Shakoor A (1996) An investigation of the relationship between uniaxial compressive strength
723 and degradation for selected rock types. Engineering Geology 44(1-4):213-27.
724 Kushnir ARL, Heap MJ, Baud P (2018a) Assessing the role of fractures on the permeability of the
725 Permo-Triassic sandstones at the Soultz-sous-Forêts (France) geothermal site. Geothermics
726 74:181-189.
727 Kushnir AR, Heap MJ, Baud P, Gilg HA, Reuschlé T, Lerouge C, Dezayes C, Duringer P (2018b)
728 Characterizing the physical properties of rocks from the Paleozoic to Permo-Triassic transition in
729 the Upper Rhine Graben. Geotherm Energy, 6:16.
730 Lin ML, Jeng FS, Tsai LS, Huang TH (2005) Wetting weakening of tertiary sandstones—microscopic
731 mechanism. Environmental Geology 48(2):265-75.
732 Louis L, David C, Metz V, Robion P, Menendez B, Kissel C (2005) Microstructural control on the
733 anisotropy of elastic and transport properties in undeformed sandstones. Int J Rock Mech Min Sci
734 42(7-8):911-23.
735 Louis L, Baud P, Wong TF (2009) Microstructural inhomogeneity and mechanical anisotropy associated
736 with bedding in Rothbach sandstone. Pure and Applied Geophysics 166(5-7):1063-87.
737 Magnenet V, Fond C, Genter A, Schmittbuhl J (2014) Two-dimensional THM modelling of the large
738 scale natural hydrothermal circulation at Soultz-sous-Forêts. Geotherm Energy 2(1):17.
739 Marinos V, Marinos P, Hoek E (2005) The geological strength index: applications and limitations. Bull
740 Eng Geol Environ 64:55-65.
741 Nespereira J, Blanco JA, Yenes M, Pereira D (2010) Irregular silica cementation in sandstones and its
742 implication on the usability as building stone. Engineering Geology 115(3-4):167-74.

743 Ngwenya BT, Main IG, Elphick SC, Crawford BR, Smart BG (2001) A constitutive law for low-
744 temperature creep of water-saturated sandstones. Journal of Geophysical Research: Solid
745 Earth 106:21811-21826.
746 Palchik V (1999) Influence of porosity and elastic modulus on uniaxial compressive strength in soft
747 brittle porous sandstones. Rock Mech Rock Eng 32:303-9.
748 Parks GA (1984) Surface and interfacial free energies of quartz. Journal of Geophysical Research: Solid
749 Earth 89(B6):3997-4008.
750 Paterson MS, Wong Tf (2005). Experimental rock deformation-the brittle field. Springer Science &
751 Business Media.
752 Pribnow D, Schellschmidt R (2000) Thermal tracking of upper crustal fluid flow in the Rhine Graben.
753 Geophys Res Lett 27(13):1957-1960.
754 Ranjith PG, Viete DR, Chen BJ, Perera MSA (2012) Transformation plasticity and the effect of
755 temperature on the mechanical behaviour of Hawkesbury sandstone at atmospheric pressure. Eng
756 Geol 151:120-127.
757 Rathnaweera TD, Ranjith PG, Perera MSA (2014) Salinity-dependent strength and stress–strain
758 characteristics of reservoir rocks in deep saline aquifers: an experimental study. Fuel 122:1-11.
759 Rao QH, Wang Z, Xie HF, Xie Q (2007). Experimental study of mechanical properties of sandstone at
760 high temperature. Journal of Central South University of Technology 14(1):478-483.
761 Rocscience Inc. (2017) https://www.rocscience.com.
762 Rutter EH, Mainprice DH (1978) The effect of water on stress relaxation of faulted and unfaulted
763 sandstone. In Rock Friction and Earthquake Prediction (pp. 634-654). Birkhäuser, Basel.
764 Sammis CG, Ashby MF (1986) The failure of brittle porous solids under compressive stress states. Acta
765 Metallurgica 34(3):511-26.
766 Sausse J, Fourar M, Genter A (2006). Permeability and alteration within the Soultz granite inferred from
767 geophysical and flow log analysis. Geothermics 35(5-6):544-560.
768 Scholz CH (1968) Microfracturing and the inelastic deformation of rock in compression. Journal of
769 Geophysical Research 73:1417-1432.
770 Scheiber J, Nitschke F, Seibt A, Genter A (2012) Geochemical and mineralogical monitoring of the
771 geothermal power plant in Soultz-sous-Forêts (France). In Proceedings of the 37th Workshop on
772 Geothermal Reservoir Engineering (pp. 1033-1042).
773 Schultz RA (1996) Relative scale and the strength and deformability of rock masses. J Struct Geol
774 18(9):1139–1149.
775 Shakoor A, Barefield EH (2009) Relationship between unconfined compressive strength and degree of
776 saturation for selected sandstones. Environmental & Engineering Geoscience 15(1):29-40.
777 Shukla R, Ranjith PG, Choi SK, Haque A, Yellishetty M, Hong L (2013) Mechanical behaviour of
778 reservoir rock under brine saturation. Rock Mech Rock Eng 46:83-93.

779 Siedel H, Pfefferkorn S, von Plehwe-Leisen E, Leisen H (2010) Sandstone weathering in tropical
780 climate: results of low-destructive investigations at the temple of Angkor Wat, Cambodia.
781 Engineering Geology 115(3-4):182-92.
782 Singh TN, Singh SK, Mishra A, Singh PK, Singh, VK (1999) Effect of acidic water on physico-
783 mechanical behaviour of rock. Indian Journal of Engineering and Material Sciences 6:66-72.
784 Tang SB, Yu CY, Heap MJ, Chen PZ, Ren YG (2018) The Influence of Water Saturation on the Short-
785 and Long-Term Mechanical Behavior of Red Sandstone. Rock Mechanics and Rock Engineering
786 1-19.
787 Ulusay R, Hudson J (2007) The Complete ISRM Suggested Methods for Rock Characterization, Testing
788 and Monitoring: 1974-2006, Antalya, Turkey, Elsevier.
789 Vásárhelyi B, Ván P (2006) Influence of water content on the strength of rock. Engineering Geology
790 84(1-2):70-4.
791 Vernoux JF, Genter A, Razin P, Vinchon C (1995) Geological and petrophysical parameters of a deep
792 fractured sandstone formation as applied to geothermal exploitation. BRGM Report 38622:70.
793 Vidal J, Genter A, Schmittbuhl J (2015) How do permeable fractures in the Triassic sediments of
794 Northern Alsace characterize the top of hydrothermal convective cells? Evidence from Soultz
795 geothermal boreholes (France). Geotherm Energy 3:8.
796 Vidal J, Genter A, Schmittbuhl J (2016) Pre-and post-stimulation characterization of geothermal well
797 GRT-1, Rittershoffen, France: insights from acoustic image logs of hard fractured
798 rock. Geophysical Journal International 206:845-860.
799 Vidal J, Genter A, Chopin F (2017) Permeable fracture zones in the hard rocks of the geothermal
800 reservoir at Rittershoffen, France. Journal of Geophysical Research: Solid Earth.
801 Vidal J, Genter A (2018) Overview of naturally permeable fractured reservoirs in the central and
802 southern Upper Rhine Graben: Insights from geothermal wells. Geothermics 74:57-73.
803 Villeneuve M, Heap MJ, Kushnir ARL, Qin T, Baud P, Zhou G, Xu T (2018) Estimating in-situ rock
804 mass strength and elastic modulus of granite from the Soultz-sous-Forêts geothermal reservoir
805 (France). Geotherm Energy 6:11.
806 Wasantha PL, Ranjith PG (2014) Water-weakening behavior of Hawkesbury sandstone in brittle regime.
807 Engineering Geology 178:91-101.
808 Wong Tf, David C, Zhu W (1997) The transition from brittle faulting to cataclastic flow in porous
809 sandstones: Mechanical deformation. Journal of Geophysical Research: Solid Earth
810 102(B2):3009-25.
811 Yang SQ, Jiang Y (2010). Triaxial mechanical creep behavior of sandstone. Mining Science and
812 Technology (China), 20(3), 339-349.
813 Zang A, Wagner CF, Dresen G (1996) Acoustic emission, microstructure, and damage model of dry and
814 wet sandstone stressed to failure. Journal of Geophysical Research: Solid Earth 101(B8):17507-
815 21.

816 Zhu W, Baud P, Wong Tf (2010) Micromechanics of cataclastic pore collapse in limestone. Journal of
817 Geophysical Research: Solid Earth 115(B4) https://doi.org/10.1029/2009JB006610.
818 Zhu W, Baud P, Vinciguerra S, Wong Tf (2011). Micromechanics of brittle faulting and cataclastic flow
819 in Alban Hills tuff. *Journal of Geophysical Research: Solid Earth 116*(B6).
820 Zhu W, Baud P, Vinciguerra S, Wong Tf (2016). Micromechanics of brittle faulting and cataclastic flow
821 in Mount Etna basalt. Journal of Geophysical Research: Solid Earth 121(6):4268-4289.

Figures

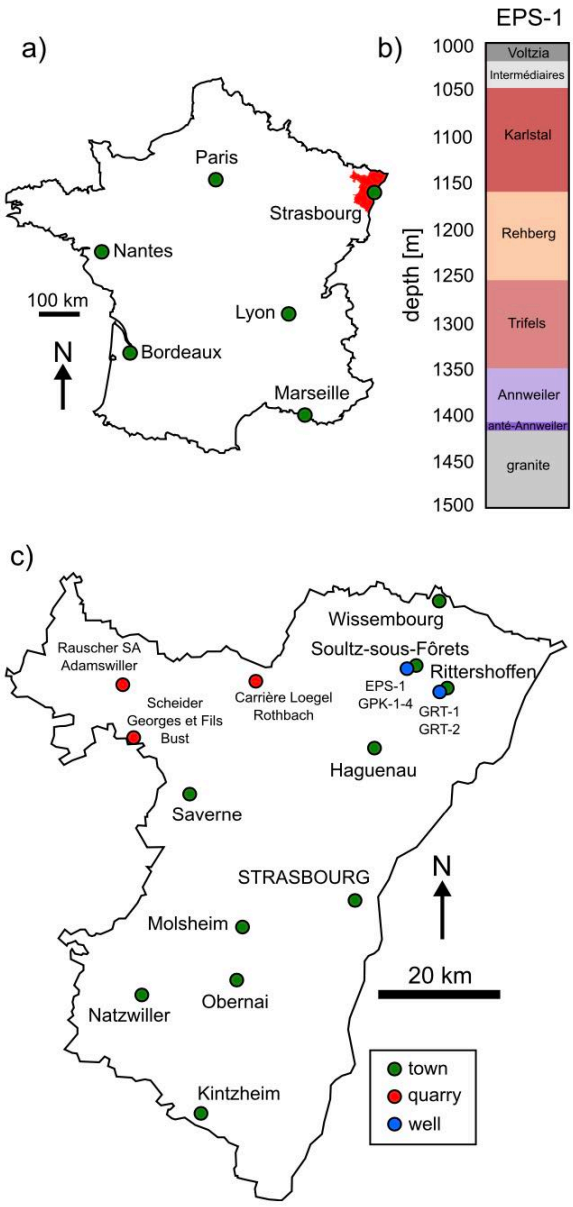

Figure 1. (a) Map of France showing the location of the Bas-Rhin (Lower Rhine) department of Alsace (in red). (b) Stratigraphic column showing the units within the Buntsandstein from exploration well EPS-1 at Soultz-sous-Forêts (Alsace, France). The granite basement is encountered at a depth of 1417 m. Depths are measured depths. (c) Map of the Bas-Rhin (Lower Rhine) department of Alsace (shown in red in panel (a)) showing the location of the major cities/towns (green circles), the geothermal sites of Soultz-sous-Forêts and Rittershoffen (green circles), the wells EPS-1, GPK-1-4, and GRT-1-2 (blue circles), and the locations and names of the quarries (red circles).

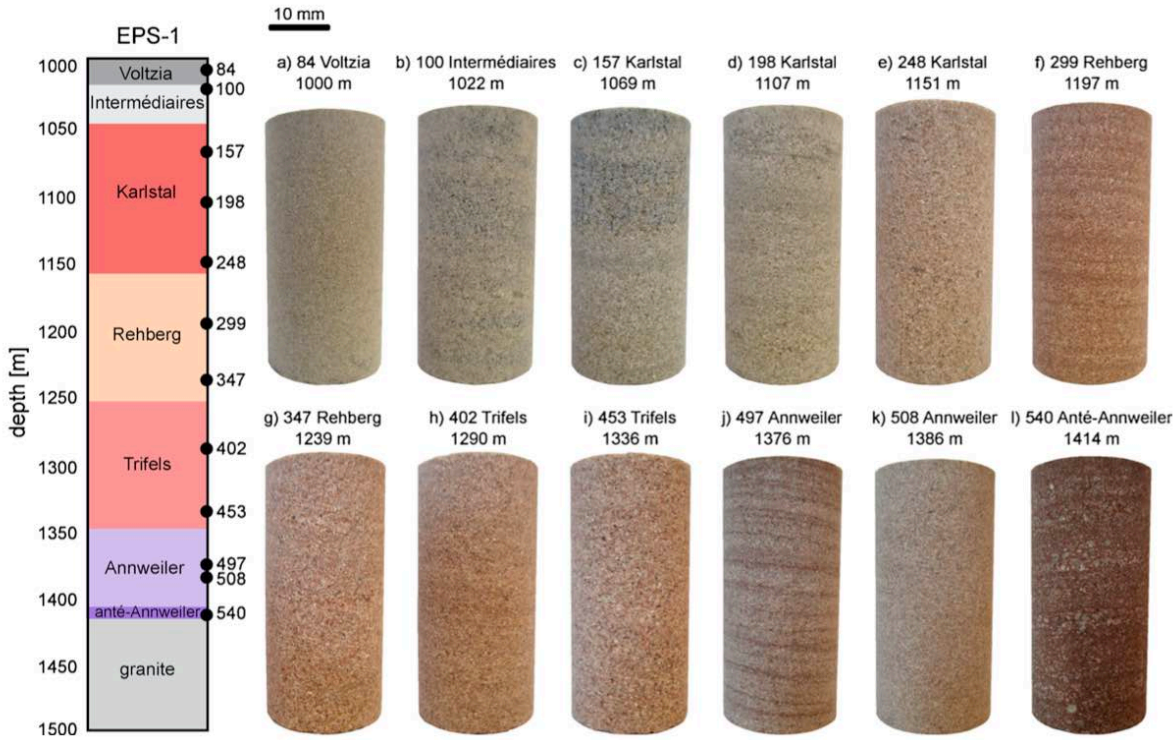

832

833 **Figure 2.** Photographs of each of the twelve sandstones (20 mm diameter core samples nominally 40
834 mm in length) sampled from exploration well EPS-1 at Soultz-sous-Forêts. The box number, lithological
835 unit, and depth are given above each sample. A stratigraphic column showing the units within the
836 Buntsandstein from exploration well EPS-1 at Soultz-sous-Forêts (Alsace, France) is shown on the left
837 hand side. The locations for each of the sampled depths are indicated on the stratigraphic column.

838

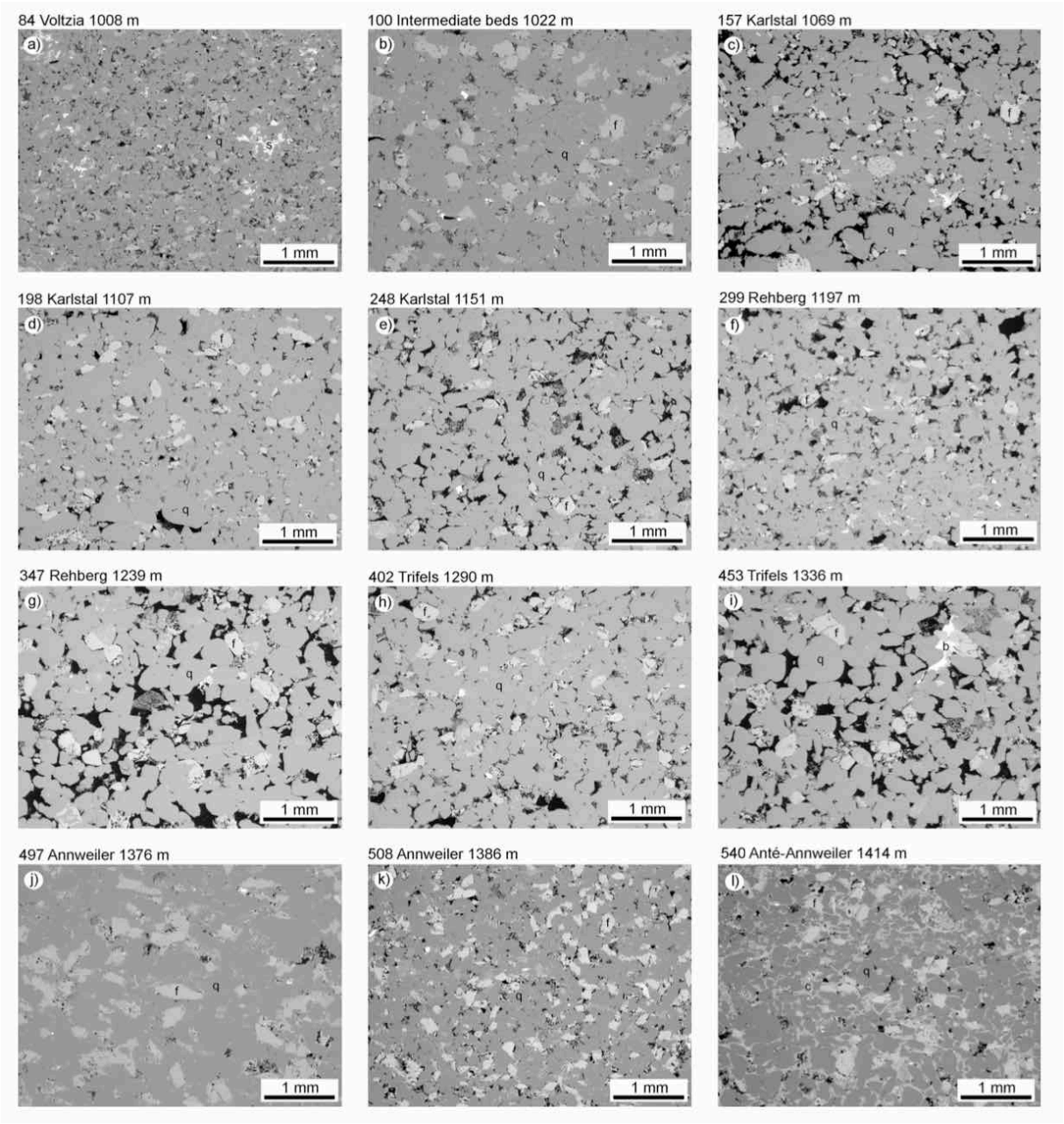

839

840 **Figure 3.** Backscattered scanning electron microscope (BSE) images for each of the twelve sandstones
841 sampled from exploration well EPS-1 at Soultz-sous-Forêts. The box number, lithological unit, and
842 depth are given above each image. q – quartz; f – feldspar; s – siderite; b – barite; c – clay.

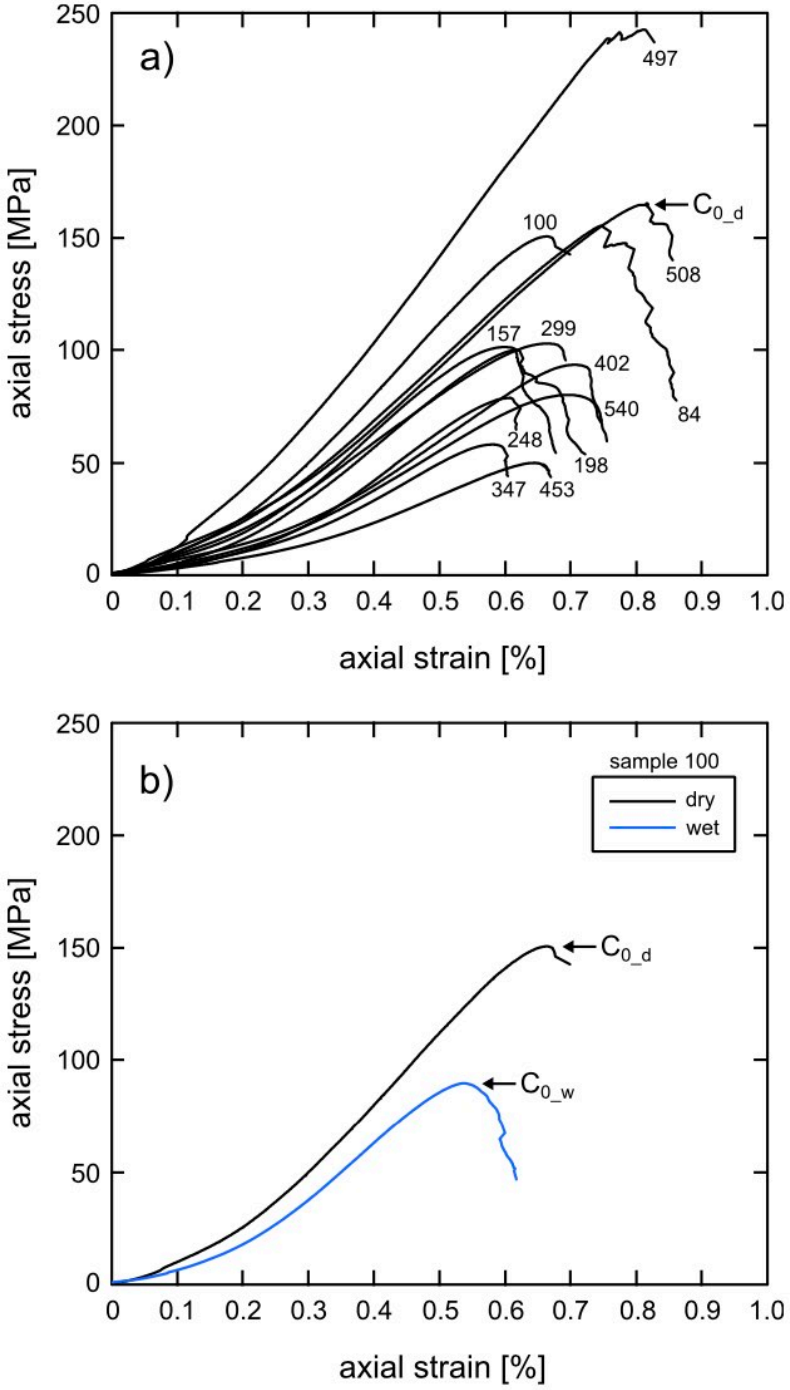

Figure 4. (a) Representative dry uniaxial stress-strain curves for each of the twelve sandstones sampled from exploration well EPS-1 at Soultz-sous-Forêts. Number next to each curve indicates the box number (see Table 3). The dry uniaxial compressive strength, C_{0_d}, is labelled for one of the curves. (b) Representative dry (black curve) and wet (blue curve) uniaxial stress-strain curves for samples taken from box number 100 (see Table 3). The dry uniaxial compressive strength, C_{0_d}, and the wet uniaxial compressive strength, C_{0_w}, are labelled on the corresponding curves.

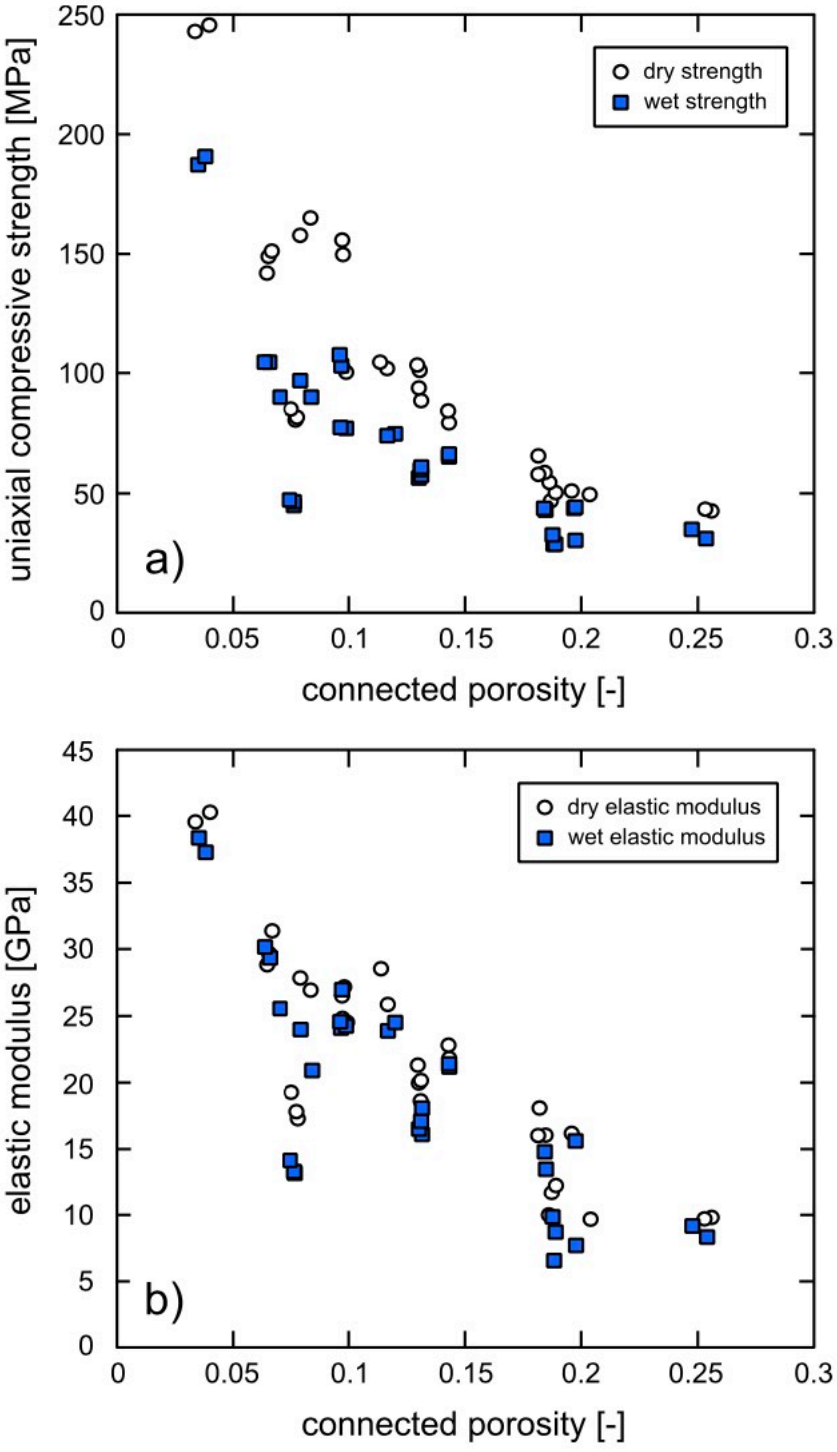

Figure 5. (a) Dry (white circles) and wet (blue squares) uniaxial compressive strength for the twelve sandstones sampled from exploration well EPS-1 at Soultz-sous-Forêts and the three quarry rocks as a function of connected porosity. (b) Dry (white circles) and wet (blue squares) elastic modulus for the twelve sandstones sampled from exploration well EPS-1 at Soultz-sous-Forêts and the three quarry rocks as a function of connected porosity.

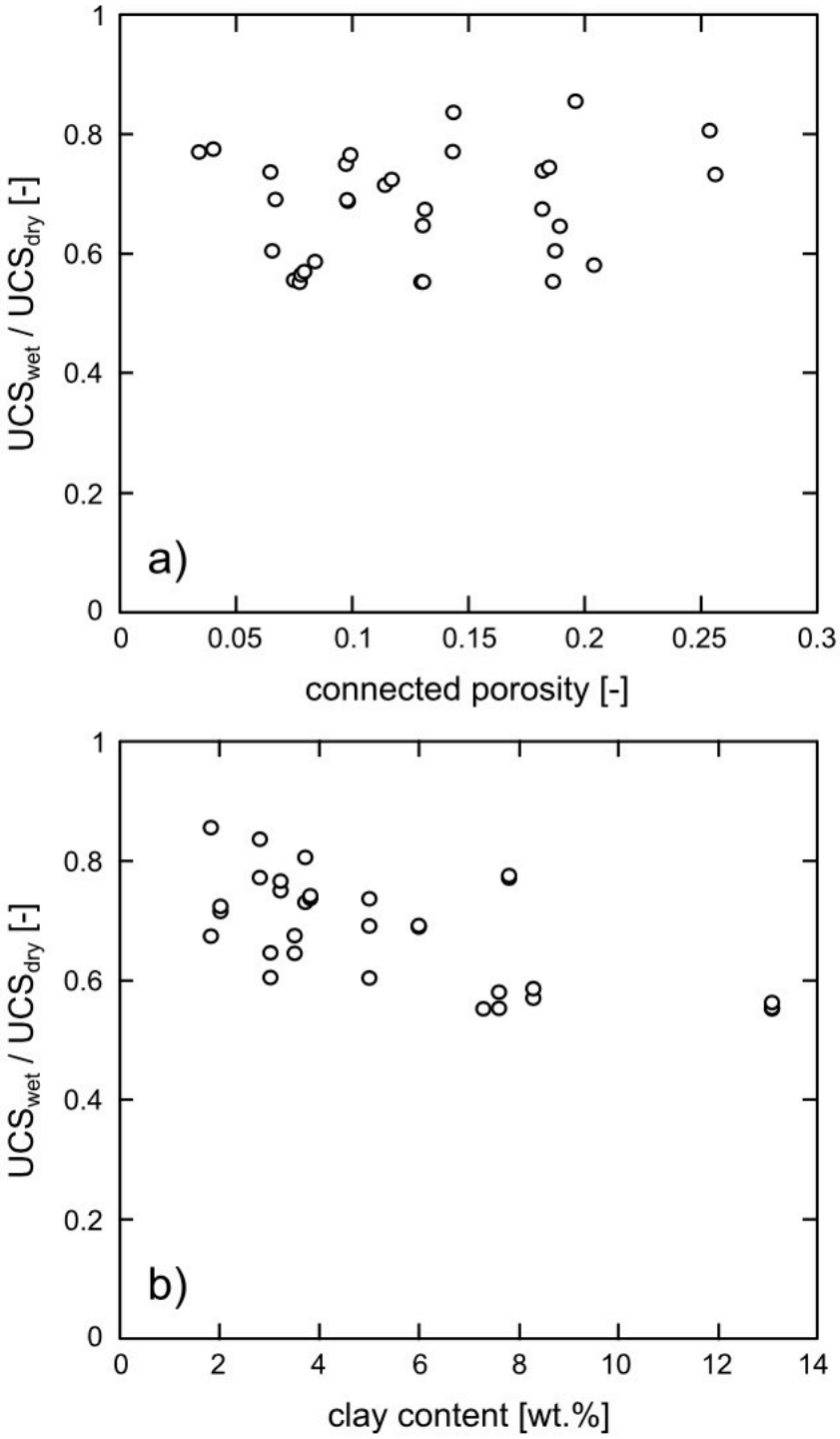

856

857 **Figure 6.** (a) The ratio of wet to dry uniaxial compressive strength for the twelve sandstones sampled
858 from exploration well EPS-1 at Soultz-sous-Forêts and the three quarry rocks as a function of connected
859 porosity. (b) The ratio of wet to dry uniaxial compressive strength for the twelve sandstones sampled
860 from exploration well EPS-1 at Soultz-sous-Forêts and the three quarry rocks as a function of clay
861 content (clay content is the wt.% of muscovite/illite-smectite; Table 1).

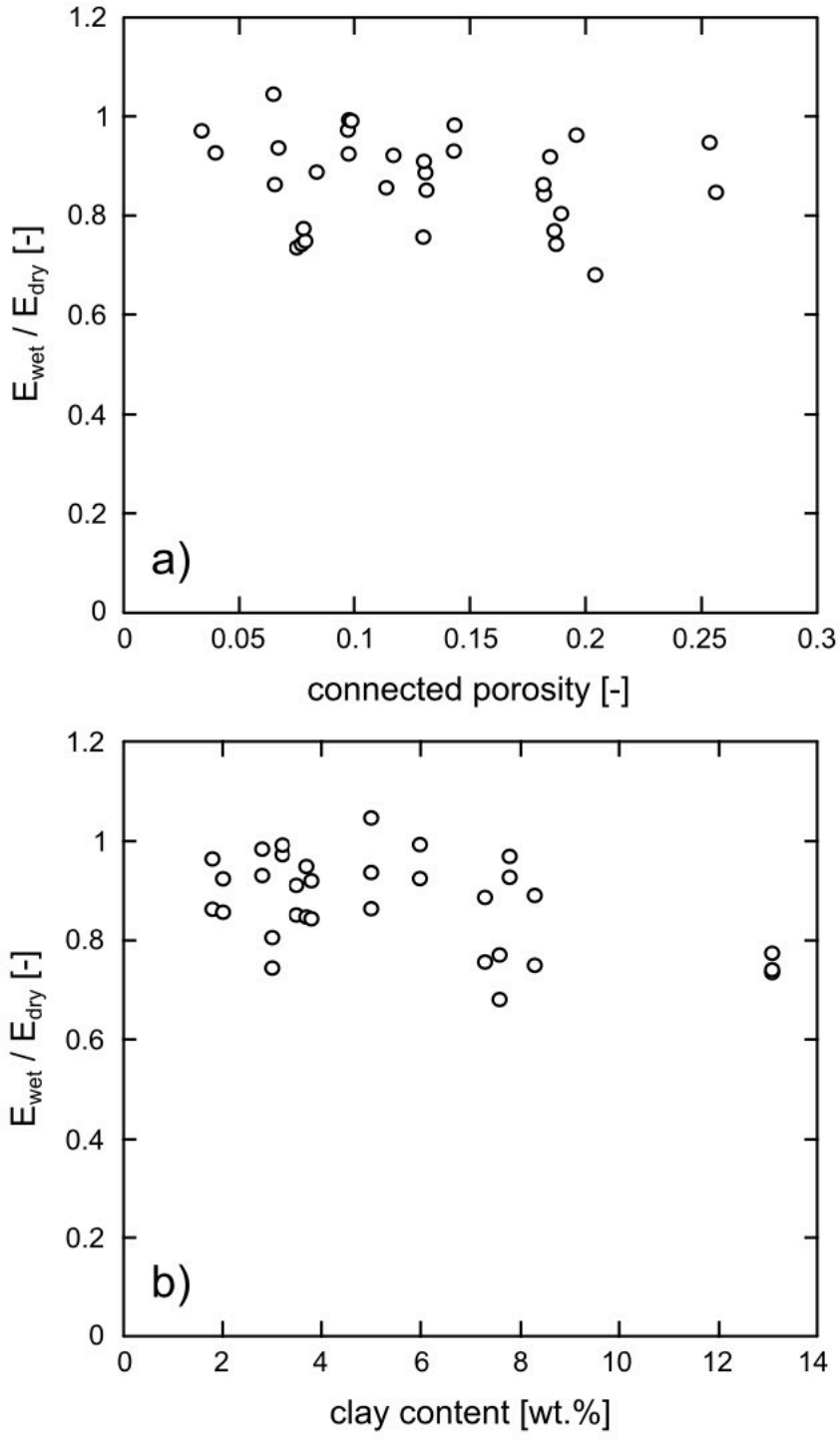

862

863 **Figure 7.** (a) The ratio of wet to dry elastic modulus for the twelve sandstones sampled from exploration
864 well EPS-1 at Soultz-sous-Forêts and the three quarry rocks as a function of connected porosity. (b) The
865 ratio of wet to dry elastic modulus for the twelve sandstones sampled from exploration well EPS-1 at
866 Soultz-sous-Forêts and the three quarry rocks as a function of clay content (clay content is the wt.% of
867 muscovite/illite-smectite; Table 1).

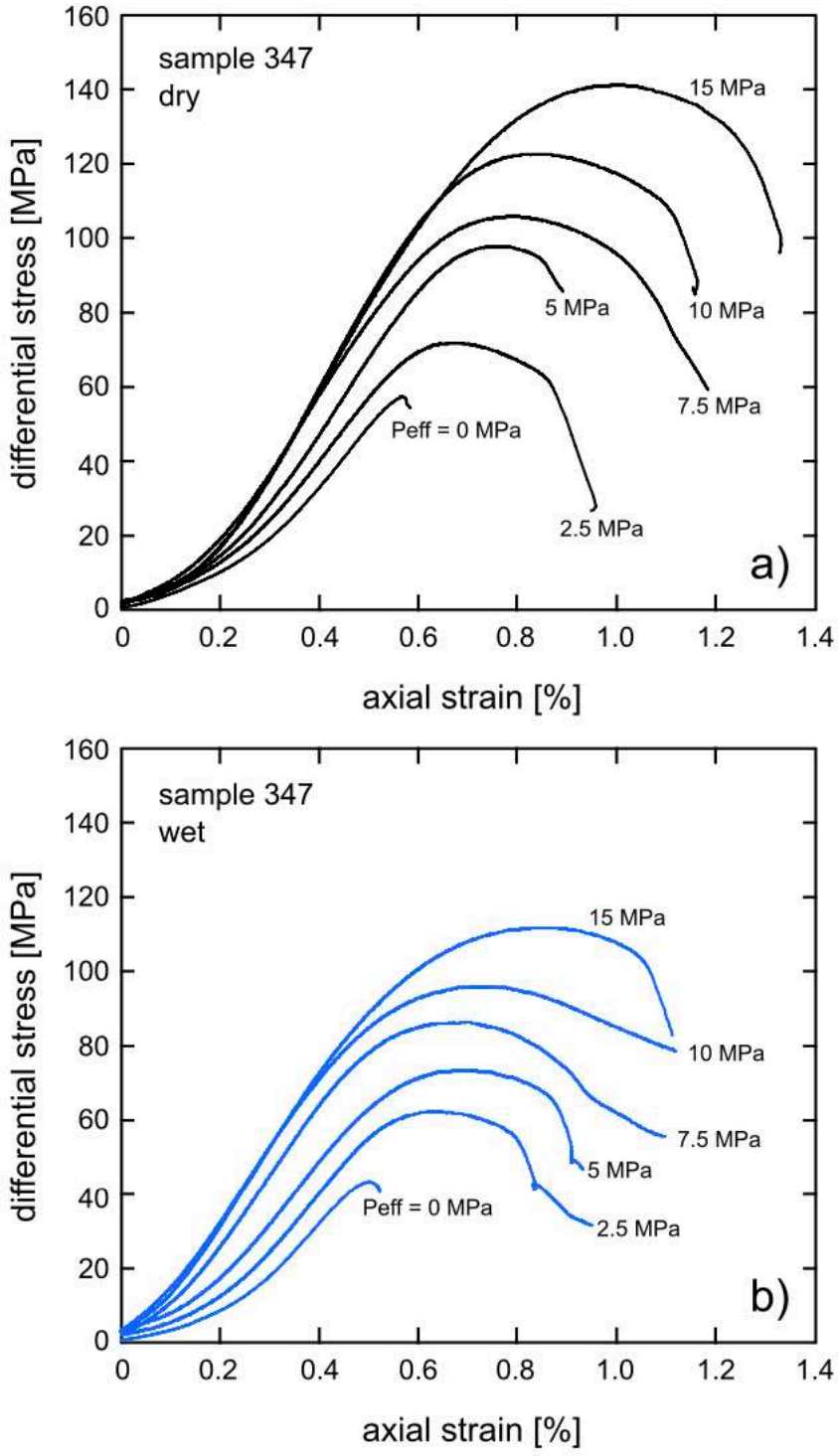

868

869 **Figure 8**. (a) Dry triaxial stress-strain curves for samples taken from box number 347 (from the *Rehberg*
870 unit; depth = 1239 m) deformed at different effective pressures (the effective pressure, $Peff$, is indicated
871 next to the curves). (b) Wet triaxial stress-strain curves for samples taken from box number 347 (from
872 the *Rehberg* unit; depth = 1239 m) deformed at different effective pressures (the effective pressure,
873 $Peff$, is indicated next to the curves).

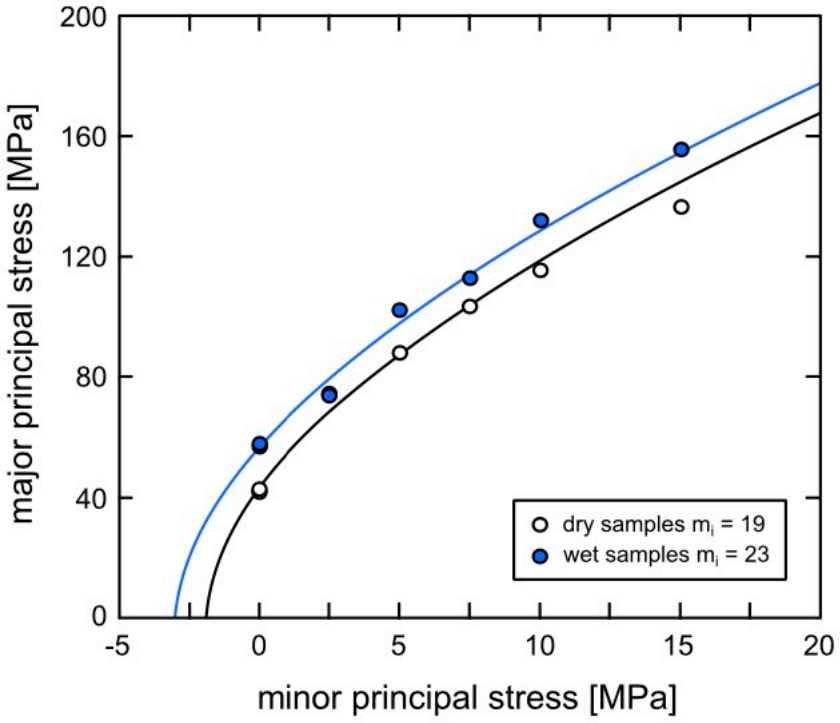

874

875 **Figure 9**. Triaxial data for wet and dry *Rehberg* unit (depth = 1239 m) plotted in principal stress space
876 with the intact Hoek-Brown failure criterion fits using Equation 2 (for the dry data) and Equation 3 (for
877 the wet data). The best-fit m_i values for the dry and wet samples are given on the figure.

878

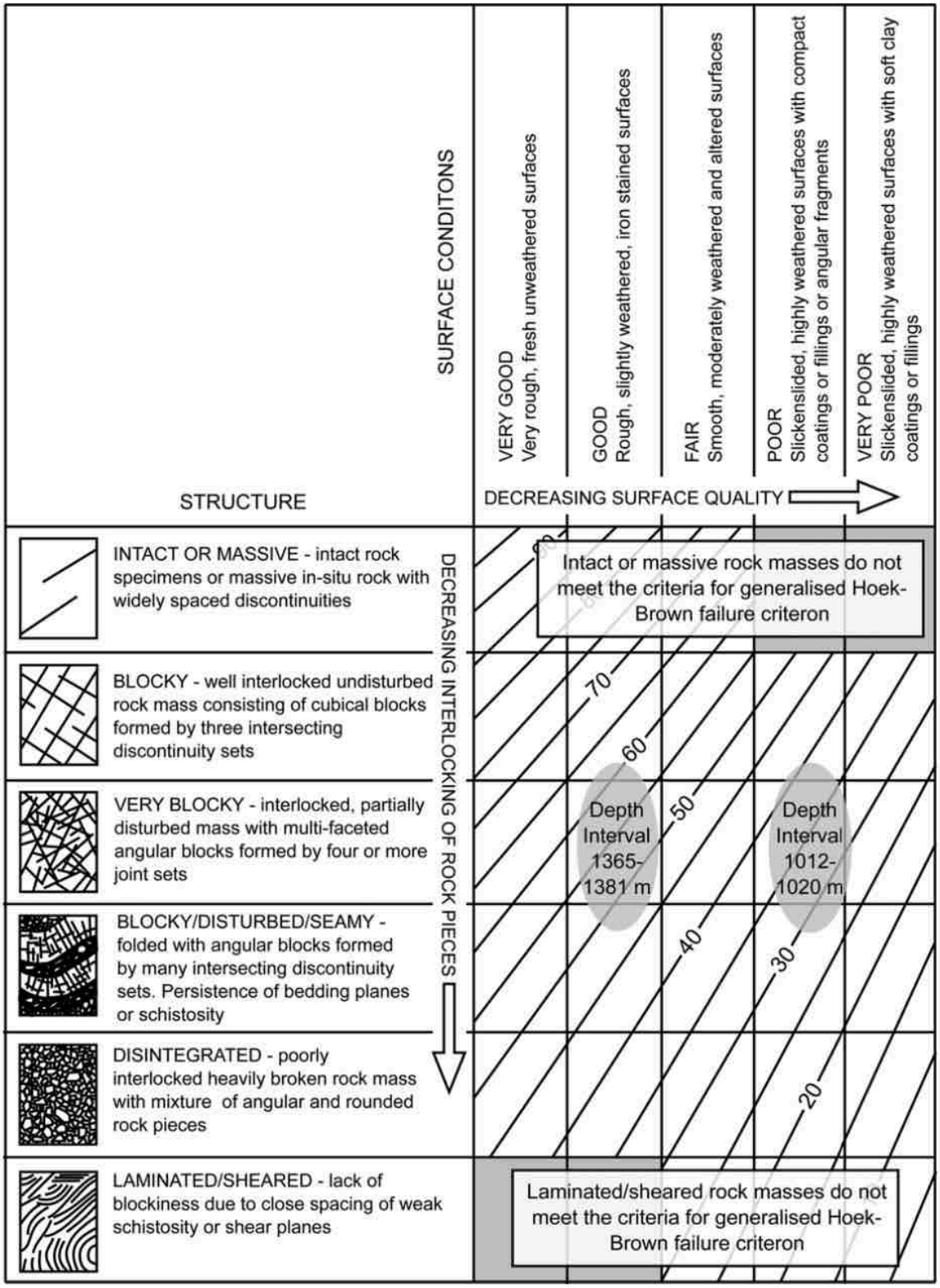

879

880 **Figure 10**. Geological Strength Index (GSI) lookup chart (modified from Marinos et al., 2005) showing
881 the assessed GSI values for two rock mass intervals (see text for details). See Table 5 for rock mass
882 descriptions based on core logging. Note that the highest and lowest category should not be used for the
883 generalised Hoek-Brown failure criterion (as indicated on the figure).

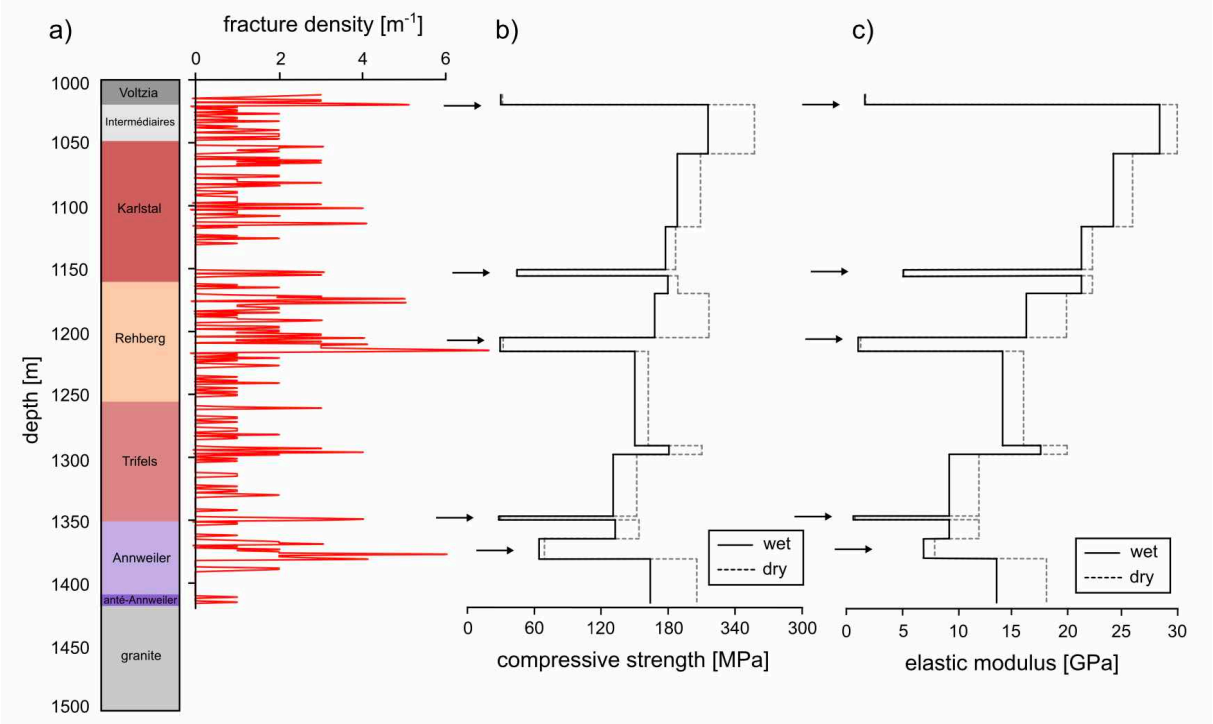

884

885 **Figure 11**. (a) Stratigraphic column showing the units within the Buntsandstein from exploration well
886 EPS-1 at Soultz-sous-Forêts next to the fracture density data for the core. (b) Wet (black line) and dry
887 (grey dashed line) rock mass compressive strength for the Bundsandstein over the depth interval 1012-
888 1416 m. (c) Wet (black line) and dry (grey dashed line) rock mass elastic modulus for the Bundsandstein
889 over the depth interval 1012-1416 m. The black arrows indicate the five fractured zones.

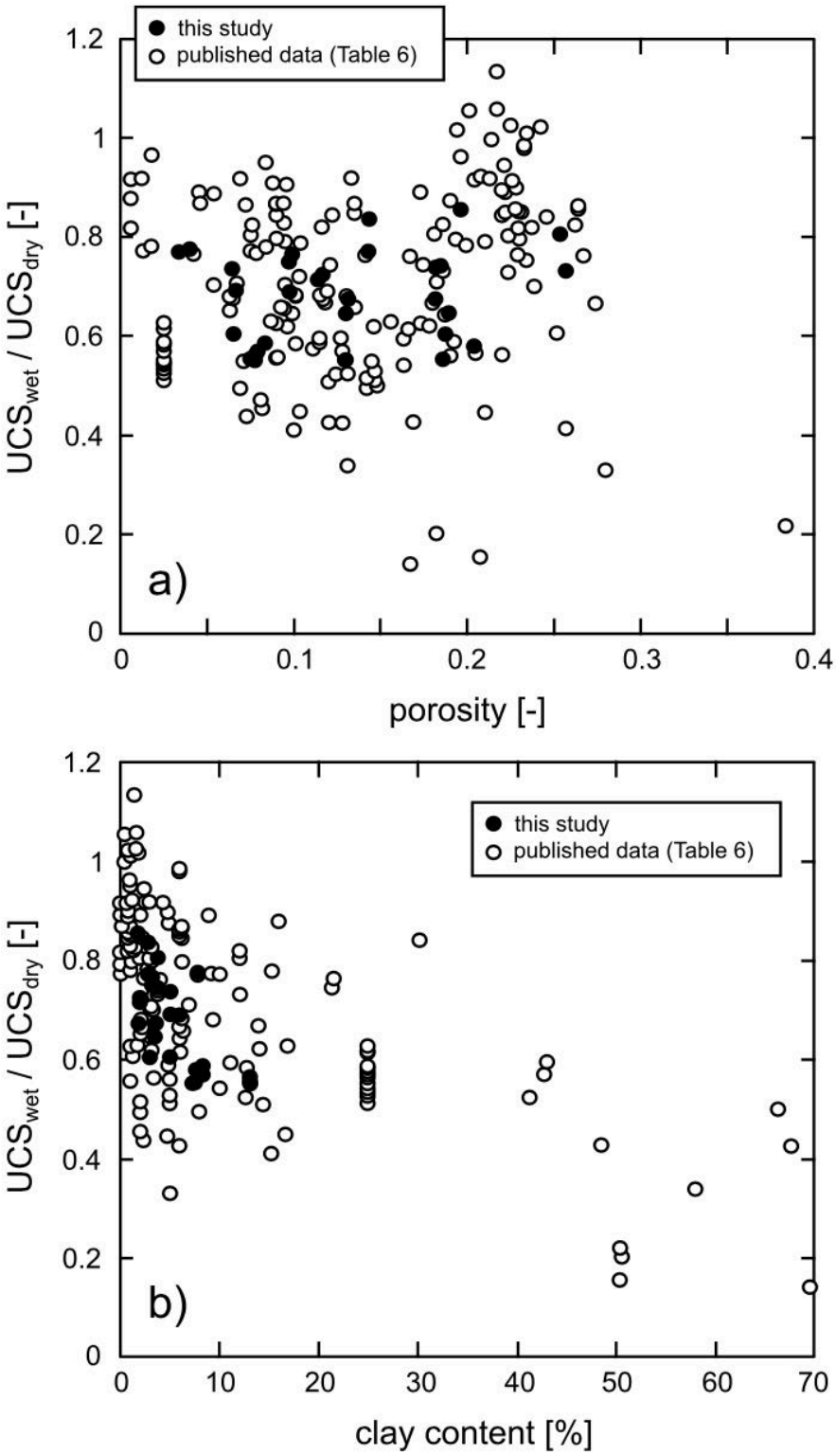

Figure 12. (a) The ratio of wet to dry uniaxial compressive strength for the data unique to this study (Table 3) and data from published studies (Table 6) as a function of connected porosity. (a) The ratio of wet to dry uniaxial compressive strength for the data unique to this study (Table 3) and data from published studies (Table 6) as a function of clay content.

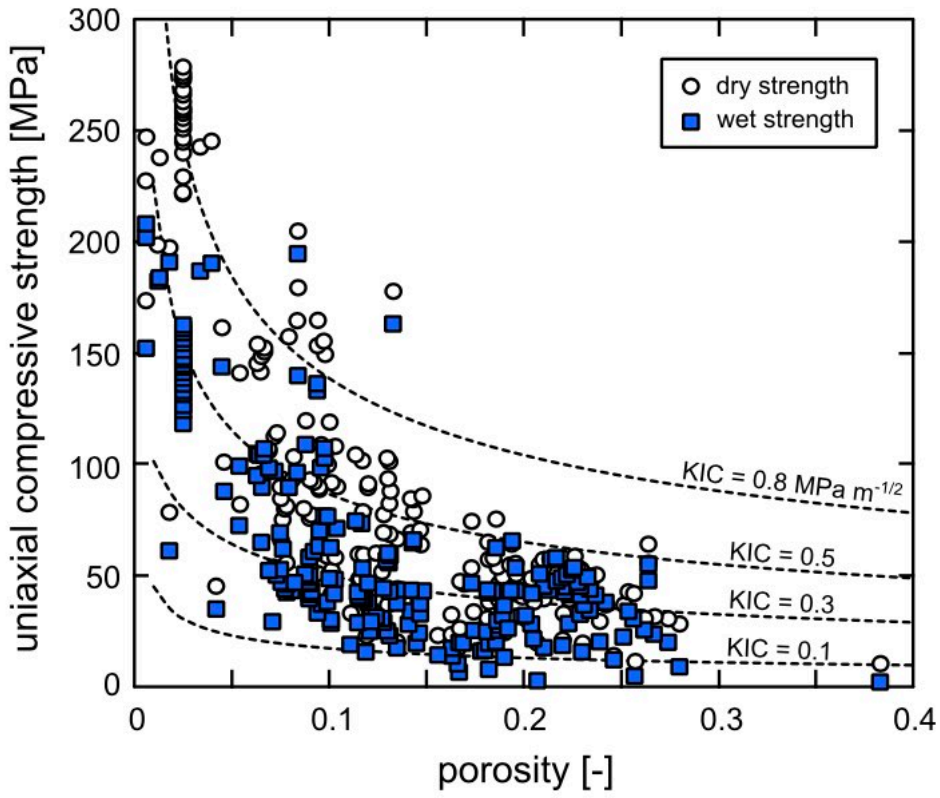

895

896 **Figure 13**. Dry (white circles) and wet (blue squares) uniaxial compressive strength data (data unique
897 to this study (Table 3) and published data (Table 6)) as a function of porosity. Modelled curves, using
898 Equation (15), show curves of uniaxial compressive strength as a function of porosity for a fixed pore
899 radius (125 μm) and different values of K_{IC} (K_{IC} = 0.1, 0.3, 0.5, and 0.8 MPa $m^{-1/2}$) (see text for details).

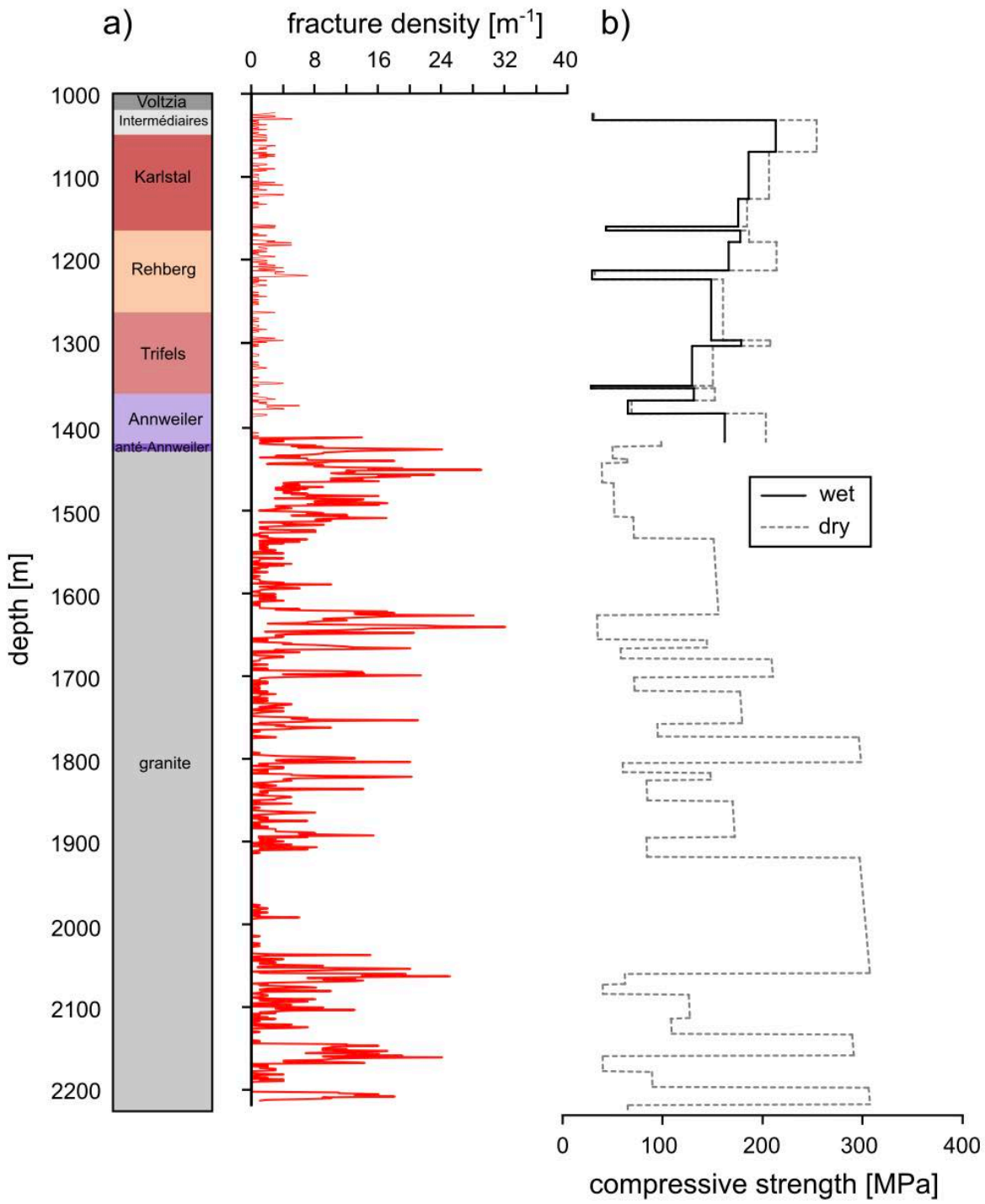

900

901 **Figure 14**. (a) Stratigraphic column of exploration well EPS-1 at Soultz-sous-Forêts (from 1012 to 2200
902 m) next to the fracture density data for the core. (b) Wet (black line) and dry (grey dashed line) rock
903 mass compressive strength. Note that dry and wet values are given for the Bundsandstein (interval 1012-
904 1416 m) only.

905

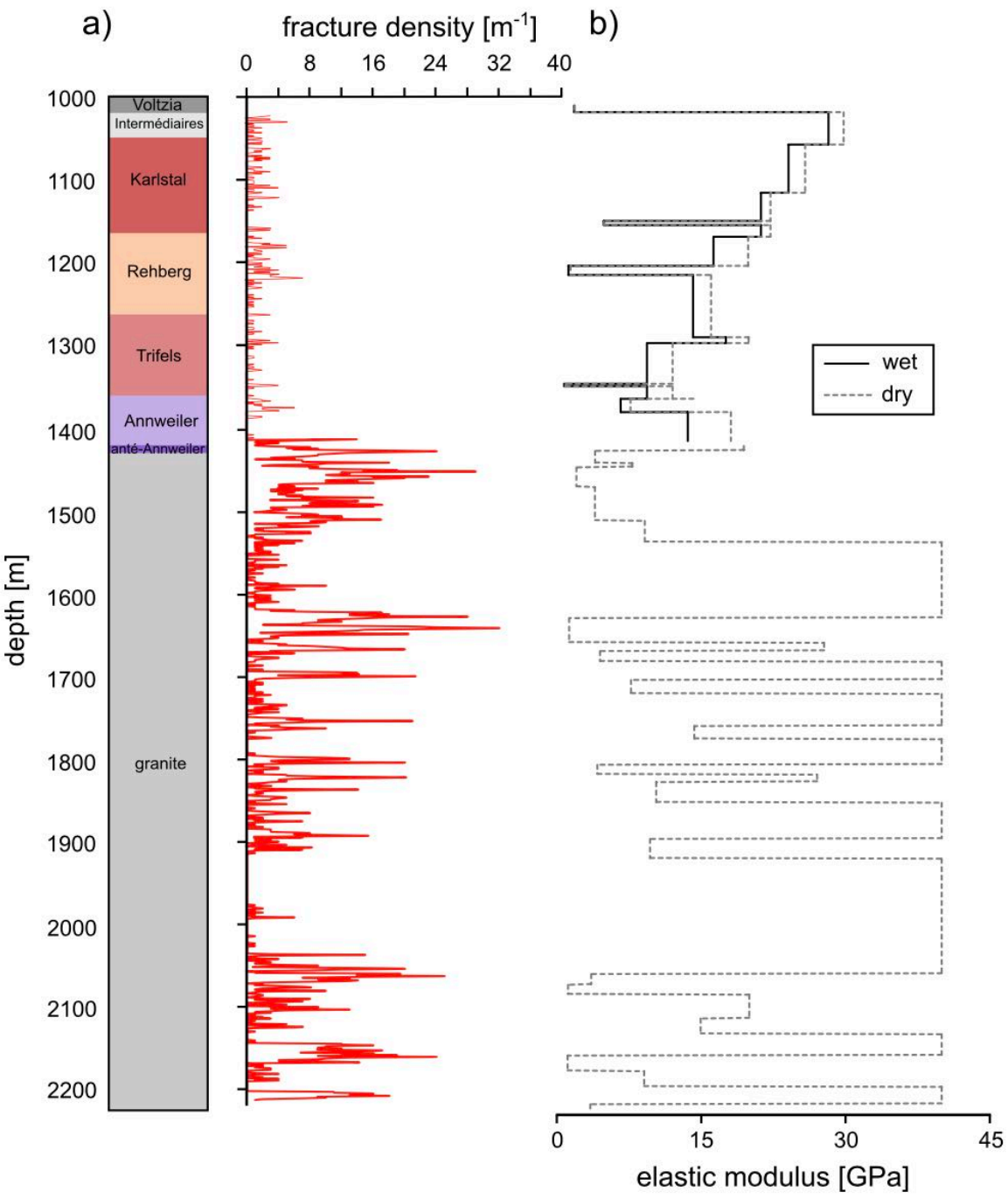

906

907 **Figure 15**. (a) Stratigraphic column of exploration well EPS-1 at Soultz-sous-Forêts (from 1012 to 2200
908 m) next to the fracture density data for the core. (b) Wet (black line) and dry (grey dashed line) rock
909 mass elastic modulus. Note that dry and wet values are given for the Bundsandstein (interval 1012-1416
910 m) only.

911

912 **Table 1.** X-ray powder diffraction (XRPD) analysis showing quantitative bulk mineralogical
913 composition for the twelve sandstones sampled from exploration well EPS-1 at the Soultz-sous-Forêts
914 geothermal site and the three quarry rocks. Values in wt.%. Data from Heap et al. (2017).
915

Box number	Depth (m)	Unit	Quartz	Orthoclase	Microcline	Muscovite Illite-smectite	Dolomite	Siderite	Hematite	Kaolinite	Chlorite
84	1008	Voltzia	74.5 ± 1.6	3.7 ± 1.9	9.3 ± 0.8	6.0 ± 2.9	4.7 ± 0.1	1.9 ± 0.2	-	-	-
100	1022	Intermédiaires	78.9 ± 1.7	5.6 ± 0.0	9.7 ± 0.5	5.0 ± 2.5	1.0 ± 0.3	-	-	-	-
157	1069	Karlstal	89.2 ± 0.4	4.6 ± 1.1	4.0 ± 1.7	2.0 ± 0.8	0.2 ± 0.1	-	-	-	-
198	1107	Karlstal	89.0 ± 1.1	3.2 ± 0.2	4.6 ± 0.0	3.2 ± 1.3	-	-	-	-	-
248	1151	Karlstal	90.7 ± 1.2	1.9 ± 0.1	4.5 ± 0.2	2.8 ± 1.3	-	-	0.2 ± 0.1	-	-
299	1197	Rehberg	83.4 ± 2.6	1.7 ± 0.2	7.4 ± 0.5	7.3 ± 3.2	-	-	0.5 ± 0.1	-	-
347	1239	Rehberg	87.8 ± 1.3	2.4 ± 0.0	5.9 ± 0.1	3.8 ± 1.5	-	-	0.3 ± 0.0	-	-
402	1290	Trifels	86.7 ± 1.6	3.0 ± 0.8	6.6 ± 0.3	3.5 ± 2.1	-	-	0.3 ± 0.0	-	-
453	1336	Trifels	82.3 ± 1.7	4.3 ± 0.6	9.4 ± 0.4	3.0 ± 1.8	0.8 ± 0.0	-	0.3 ± 0.1	-	-
497	1376	Annweiler	73.3 ± 3.0	4.8 ± 0.4	11.1 ± 0.6	7.8 ± 3.9	2.1 ± 0.0	-	0.9 ± 0.1	-	-
508	1386	Annweiler	70.6 ± 2.8	6.9 ± 1.1	13.8 ± 0.5	8.3 ± 4.5	-	-	0.5 ± 0.1	-	-
540	1414	Anté-Annweiler	66.4 ± 4.0	4.4 ± 0.9	10.7 ± 0.7	13.1 ± 6.0	4.2 ± 0.5	-	1.4 ± 0.1	-	-
Rothbach	Quarry	Karlstal	82.8 ± 0.5	7.8 ± 0.2	7.1 ± 0.2	1.8 ± 0.5	-	-	0.4 ± 0.2	-	-
Adamswiller	Quarry	Voltzia	71.8 ± 0.6	10.4 ± 0.2	11.8 ± 0.5	3.7 ± 1.0	-	-	0.7 ± 0.2	-	1.7 ± 0.2
Bust	Quarry	Voltzia	67.4 ± 1.0	10.4 ± 0.2	13.5 ± 0.5	4.0 ± 1.0	0.5 ± 0.1	-	0.5 ± 0.1	3.6 ± 0.5	-

916
917

Table 2. Average connected porosity, average grain diameter, specific surface area, average dry and wet P-wave velocity, and average permeability for each of the twelve sandstones sampled from exploration well EPS-1 at the Soultz-sous-Forêts geothermal site and the three quarry rocks. Physical property data taken from Heap et al. (2017). Elastic wave velocities were measured at room pressure and permeabilities were measured under a confining pressure of 1 MPa. Grain size data for Rothbach and Adamswiller sandstone from Louis et al. (2005; 2009) and David et al. (1994), respectively.

Box number	Depth (m)	Unit	Average connected porosity	Average grain diameter (μm)	Specific surface area (m^2/kg)	Average dry P-wave velocity (km/s)	Average wet P-wave velocity (km/s)	Average permeability (m^2)
84	1008	Voltzia	0.096	142	1442	3.7	4.4	2.82×10^{-18}
100	1022	Intermédiaires	0.065	306	665	3.6	4.6	6.45×10^{-18}
157	1069	Karlstal	0.117	424	204	3.4	4.3	1.33×10^{-16}
198	1107	Karlstal	0.097	192	1485	3.2	4.4	7.95×10^{-17}
248	1151	Karlstal	0.144	294	1175	3.1	4.1	5.24×10^{-15}
299	1197	Rehberg	0.130	332	1888	3.4	4.1	1.15×10^{-17}
347	1239	Rehberg	0.185	367	1098	2.9	3.8	4.66×10^{-15}
402	1290	Trifels	0.131	259	1349	3.1	4.1	2.37×10^{-16}
453	1336	Trifels	0.189	361	1174	2.7	3.7	9.06×10^{-15}
497	1376	Annweiler	0.034	291	2024	4.1	5.1	2.08×10^{-18}
508	1386	Annweiler	0.082	199	2777	3.4	4.4	2.12×10^{-18}
540	1414	Anté-Annweiler	0.075	379	6170	2.9	4.2	7.89×10^{-18}
Rothbach	Quarry	Karlstal	0.191	100-150 (low-porosity layers) 200-250 (high-porosity layers)	-	3.4	3.9	6.94×10^{-14}
Adamswiller	Quarry	Voltzia	0.253	120	-	2.3	3.0	3.54×10^{-13}
Bust	Quarry	Voltzia	0.192	-	-	2.8	3.2	4.82×10^{-14}

926 **Table 3.** Summary of the dry and wet uniaxial compressive strength experiments performed on the
927 twelve sandstones sampled from exploration well EPS-1 at the Soultz-sous-Forêts geothermal site and
928 the three quarry rocks. Also included are the connected porosity, average grain diameter, and clay
929 content (average grain diameter and clay content taken from Heap et al., 2017).

930

Box number	Depth (m)	Unit	Connected porosity	Average grain diameter (µm)	Clay content (wt.%)	Dry UCS (C_{o_d}) (MPa)	Wet UCS (C_{o_w}) (MPa)	Elastic modulus (GPa)
84	1008	Voltzia	0.098	142	6.0	149.3	-	27.2
84	1008	Voltzia	0.097	142	6.0	155.4	-	26.6
84	1008	Voltzia	0.096	142	6.0	-	107.4	24.6
84	1008	Voltzia	0.097	142	6.0	-	102.8	27.0
100	1022	Intermédiaires	0.067	306	5.0	150.7	-	31.4
100	1022	Intermédiaires	0.065	306	5.0	148.5	-	29.7
100	1022	Intermédiaires	0.065	306	5.0	141.7	-	28.9
100	1022	Intermédiaires	0.070	306	5.0	-	89.9	25.6
100	1022	Intermédiaires	0.066	306	5.0	-	104.2	29.4
100	1022	Intermédiaires	0.064	306	5.0	-	104.4	30.2
157	1069	Karlstal	0.117	424	2.0	101.6	-	25.9
157	1069	Karlstal	0.114	424	2.0	104.3	-	28.6
157	1069	Karlstal	0.117	424	2.0	-	73.6	23.9
157	1069	Karlstal	0.120	424	2.0	-	74.6	24.5
198	1107	Karlstal	0.099	192	3.2	100.2	-	24.5
198	1107	Karlstal	0.097	192	3.2	102.6	-	24.8
198	1107	Karlstal	0.097	192	3.2	-	76.8	24.3
198	1107	Karlstal	0.099	192	3.2	-	77.0	24.1
248	1151	Karlstal	0.143	294	2.8	79.0	-	21.8
248	1151	Karlstal	0.143	294	2.8	84.1	-	22.8

248	1151	Karlstal	0.143	294	2.8	-	66.1	21.4
248	1151	Karlstal	0.143	294	2.8	-	64.9	21.2
299	1197	Rehberg	0.130	332	7.3	103.1	-	21.3
299	1197	Rehberg	0.131	332	7.3	101.1	-	18.6
299	1197	Rehberg	0.130	332	7.3	-	55.9	16.5
299	1197	Rehberg	0.131	332	7.3	-	57.0	16.1
347	1239	Rehberg	0.185	367	3.8	58.2	-	16.1
347	1239	Rehberg	0.182	367	3.8	57.4	-	16.0
347	1239	Rehberg	0.184	367	3.8	-	43.3	14.8
347	1239	Rehberg	0.185	367	3.8	-	42.4	13.5
402	1290	Trifels	0.130	259	3.5	93.6	-	19.9
402	1290	Trifels	0.131	259	3.5	88.2	-	20.1
402	1290	Trifels	0.131	259	3.5	-	59.5	17.1
402	1290	Trifels	0.131	259	3.5	-	60.5	18.1
453	1336	Trifels	0.189	361	3.0	50.0	-	12.3
453	1336	Trifels	0.187	361	3.0	46.6	-	11.7
453	1336	Trifels	0.188	361	3.0	-	32.3	9.9
453	1336	Trifels	0.189	361	3.0	-	28.2	8.7
497	1376	Annweiler	0.034	291	7.8	242.7	-	39.6
497	1376	Annweiler	0.040	291	7.8	245.2	-	40.3
497	1376	Annweiler	0.038	291	7.8	-	190.4	37.3
497	1376	Annweiler	0.035	291	7.8	-	187.1	38.4
508	1386	Annweiler	0.084	199	8.3	164.7	-	27.0
508	1386	Annweiler	0.079	199	8.3	157.3	-	27.9
508	1386	Annweiler	0.079	199	8.3	-	96.7	24.0
508	1386	Annweiler	0.084	199	8.3	-	89.7	20.9
540	1414	Anté-Annweiler	0.077	379	13.1	80.3	-	17.8
540	1414	Anté-Annweiler	0.075	379	13.1	84.7	-	19.3

540	1414	Anté-Annweiler	0.078	379	13.1	81.3	-	17.3
540	1414	Anté-Annweiler	0.077	379	13.1	-	44.4	13.2
540	1414	Anté-Annweiler	0.075	379	13.1	-	47.0	14.2
540	1414	Anté-Annweiler	0.076	379	13.1	-	45.9	13.4
Bust	Quarry	Voltzia	0.204	-	4.0	49.1	-	9.7
Bust	Quarry	Voltzia	0.186	-	4.0	54.0	-	10.0
Bust	Quarry	Voltzia	0.198	-	4.0	-	29.9	7.7
Bust	Quarry	Voltzia	0.188	-	4.0	-	28.5	6.6
Adamswiller	Quarry	Voltzia	0.253	120	3.7	42.8	-	9.7
Adamswiller	Quarry	Voltzia	0.256	120	3.7	42.1	-	9.8
Adamswiller	Quarry	Voltzia	0.254	120	3.7	-	30.8	8.3
Adamswiller	Quarry	Voltzia	0.248	120	3.7	-	34.5	9.2
Rothbach	Quarry	Karlstal	0.196	100-250	1.8	50.5	-	16.2
Rothbach	Quarry	Karlstal	0.182	100-250	1.8	65.1	-	18.1
Rothbach	Quarry	Karlstal	0.197	100-250	1.8	-	43.2	15.6
Rothbach	Quarry	Karlstal	0.198	100-250	1.8	-	43.9	15.6

931

932

933 **Table 4.** Summary of the dry and wet triaxial compressive strength experiments performed on samples
934 taken from box number 347 (from the *Rehberg* unit).
935

Sample	Connected porosity	Condition	Confining pressure (MPa)	Pore fluid pressure (MPa)	Effective pressure (MPa)	Peak differential stress (MPa)
347_12	0.181	Dry	2.5	0	2.5	71.8
347_8	0.179	Dry	5	0	5	97.7
347_13	0.177	Dry	7.5	0	7.5	105.8
347_9	0.178	Dry	10	0	10	122.5
347_11	0.181	Dry	15	0	15	141.1
347_23	0.179	Wet	12.5	10	2.5	62.3
347_14	0.180	Wet	15	10	5	73.4
347_17	0.177	Wet	17.5	10	7.5	86.3
347_16	0.177	Wet	20	10	10	95.9
347_18	0.179	Wet	25	10	15	111.8

936

Table 5. Summary of rock mass descriptions for Geological Strength Index (GSI) assessment, and the resulting intact and rock mass strength and elastic modulus for the wet and dry sandstone units. Wet and dry intact C_o and E_i are given as averages for the rock type associated with the rock mass interval. S_{hmin} = minimum horizontal stress; UCS = uniaxial compressive strength; E_i = intact elastic modulus; E_{rm} = rock mass elastic modulus.

See Excel spreadsheet for Table 5.

944 **Table 6.** Published wet and dry uniaxial compressive strength data for sandstones. Rate in brackets for
945 the Pennant sandstone experiments (Hadizadeh and Law, 1991) is the experimental strain rate. H & L =
946 Hadizadeh and Law; H & M = Hawkins and McConnell; para = parallel to bedding; perp = perpendicular
947 to bedding.
948

Sandstone	Porosity	Clay content (%)	Dry UCS (MPa)	Wet UCS (MPa)	UCSwet / UCSdry	Reference
Fell sandstone	0.111	-	33.2	19.1	0.58	Bell (1978)
Fell sandstone	0.127	-	51.9	31.0	0.60	Bell (1978)
Fell sandstone	0.115	-	73.7	43.3	0.59	Bell (1978)
Fell sandstone	0.117	-	79.1	53.5	0.68	Bell (1978)
Fell sandstone	0.205	-	38.1	21.6	0.57	Bell (1978)
Fell sandstone	0.096	-	108.9	98.6	0.91	Bell (1978)
Fell sandstone	0.095	-	88.7	70.2	0.79	Bell (1978)
Fell sandstone	0.104	-	90.2	71.2	0.79	Bell (1978)
Fell sandstone	0.095	-	89.9	63.4	0.71	Bell (1978)
Fell sandstone	0.094	-	51.1	33.5	0.66	Bell (1978)
Fell sandstone	0.099	-	59.0	38.2	0.65	Bell (1978)
Fell sandstone	0.101	-	91.7	62.7	0.68	Bell (1978)
Fell sandstone	0.092	-	92.4	60.9	0.66	Bell (1978)
Fell sandstone	0.072	-	112.4	97.2	0.87	Bell (1978)
Fell sandstone	0.071	-	53.9	29.6	0.55	Bell (1978)
Fell sandstone	0.076	-	75.2	62.0	0.82	Bell (1978)
Fell sandstone	0.096	-	60.2	37.3	0.62	Bell (1978)
Fell sandstone	0.101	-	52.3	30.6	0.59	Bell (1978)
Fell sandstone	0.091	-	77.2	43.1	0.56	Bell (1978)
Fell sandstone	0.078	-	55.7	42.7	0.77	Bell (1978)
Fell sandstone	0.081	-	93.1	43.9	0.47	Bell (1978)
Fell sandstone	0.069	-	107.2	98.4	0.92	Bell (1978)
Fell sandstone	0.065	-	95.8	64.9	0.68	Bell (1978)
Fell sandstone	0.087	-	80.5	50.8	0.63	Bell (1978)
Pennant sandstone ($10^{-2.0}$ s^{-1})	0.025	25	257.3	143.5	0.56	H & L (1991)
Pennant sandstone ($10^{-2.0}$ s^{-1})	0.025	25	263.7	151.9	0.58	H & L (1991)
Pennant sandstone ($10^{-2.2}$ s^{-1})	0.025	25	268.3	141.3	0.53	H & L (1991)
Pennant sandstone ($10^{-2.2}$ s^{-1})	0.025	25	259.0	136.2	0.53	H & L (1991)
Pennant sandstone ($10^{-2.4}$ s^{-1})	0.025	25	263.1	162.4	0.62	H & L (1991)
Pennant sandstone ($10^{-2.4}$ s^{-1})	0.025	25	247.1	151.8	0.62	H & L (1991)
Pennant sandstone ($10^{-2.4}$ s^{-1})	0.025	25	272.9	157.3	0.58	H & L (1991)
Pennant sandstone ($10^{-2.6}$ s^{-1})	0.025	25	267.7	154.7	0.58	H & L (1991)
Pennant sandstone ($10^{-2.6}$ s^{-1})	0.025	25	274.1	161.0	0.59	H & L (1991)
Pennant sandstone ($10^{-2.9}$ s^{-1})	0.025	25	275.7	156.4	0.57	H & L (1991)

Pennant sandstone ($10^{-3.3}$ s^{-1})	0.025	25	278.5	162.6	0.58	H & L (1991)
Pennant sandstone ($10^{-3.4}$ s^{-1})	0.025	25	262.8	154.5	0.59	H & L (1991)
Pennant sandstone ($10^{-3.5}$ s^{-1})	0.025	25	253.5	159.1	0.63	H & L (1991)
Pennant sandstone ($10^{-3.6}$ s^{-1})	0.025	25	267.9	151.5	0.57	H & L (1991)
Pennant sandstone ($10^{-4.0}$ s^{-1})	0.025	25	257.2	148.0	0.58	H & L (1991)
Pennant sandstone ($10^{-4.1}$ s^{-1})	0.025	25	258.8	145.4	0.56	H & L (1991)
Pennant sandstone ($10^{-4.5}$ s^{-1})	0.025	25	246.5	143.6	0.58	H & L (1991)
Pennant sandstone ($10^{-4.6}$ s^{-1})	0.025	25	254.5	144.8	0.57	H & L (1991)
Pennant sandstone ($10^{-4.8}$ s^{-1})	0.025	25	265.9	146.9	0.55	H & L (1991)
Pennant sandstone ($10^{-4.8}$ s^{-1})	0.025	25	255.3	138.9	0.54	H & L (1991)
Pennant sandstone ($10^{-4.8}$ s^{-1})	0.025	25	244.7	138.8	0.57	H & L (1991)
Pennant sandstone ($10^{-5.4}$ s^{-1})	0.025	25	250.9	136.1	0.54	H & L (1991)
Pennant sandstone ($10^{-5.5}$ s^{-1})	0.025	25	252.5	132.7	0.53	H & L (1991)
Pennant sandstone ($10^{-5.5}$ s^{-1})	0.025	25	260.2	133.2	0.51	H & L (1991)
Pennant sandstone ($10^{-6.2}$ s^{-1})	0.025	25	240.1	131.3	0.55	H & L (1991)
Pennant sandstone ($10^{-6.8}$ s^{-1})	0.025	25	229.3	124.3	0.54	H & L (1991)
Pennant sandstone ($10^{-6.8}$ s^{-1})	0.025	25	221.7	118.4	0.53	H & L (1991)
Pennant sandstone ($10^{-7.9}$ s^{-1})	0.025	25	222.2	126.5	0.57	H & L (1991)
Applecross	0.054	3.0	141.3	99.3	0.70	H & M (1992)
Donegal Quartzite	0.013	0.0	237.9	184.0	0.77	H & M (1992)
Basal Quartzite	0.006	0.0	247.0	202.1	0.82	H & M (1992)
Brownstones	0.067	3.1	152.0	107.4	0.71	H & M (1992)
Pilton (type A)	0.006	16.0	173.3	152.2	0.88	H & M (1992)
Pilton (type B)	0.006	4.3	227.3	208.4	0.92	H & M (1992)
Upper Cromhall	0.045	0.0	161.4	143.9	0.89	H & M (1992)
Millstone Grit A	0.118	13.9	59.3	39.6	0.67	H & M (1992)
Millstone Grit B	0.116	12.0	49.0	40.2	0.82	H & M (1992)
Millstone Grit C	-	12.7	123.4	72.1	0.58	H & M (1992)
Millstone Grit D	-	9.2	127.5	98.6	0.77	H & M (1992)
Holcomb Brook Grit A	0.1	15.2	119.1	49.0	0.41	H & M (1992)
Holcomb Brook Grit B	0.103	16.7	108.1	48.6	0.45	H & M (1992)
Siliceous Sandstone	0.012	3.0	198.4	182.2	0.92	H & M (1992)
Elland Flags	0.124	12.6	59.9	31.4	0.52	H & M (1992)
Thornhill Rock A	0.12	5.9	89.9	38.4	0.43	H & M (1992)
Thornhill Rock B	0.12	14.4	91.8	46.7	0.51	H & M (1992)
Middle Coal Measures	0.13	9.4	37.1	25.3	0.68	H & M (1992)

Crackington Formation	-	15.3	298.2	232.3	0.78	H & M (1992)
Pennant A	0.073	2.3	114.2	50.0	0.44	H & M (1992)
Pennant B	0.069	7.9	106.2	52.6	0.50	H & M (1992)
Pennant C	0.082	2.0	103.4	47.0	0.46	H & M (1992)
Annan Sandstone	0.135	6.3	66.3	43.6	0.66	H & M (1992)
Penrith A	0.075	1.9	66.0	53.1	0.81	H & M (1992)
Penrith B	0.122	2.2	34.8	29.4	0.85	H & M (1992)
Penrith C	0.054	0.7	82.0	72.8	0.89	H & M (1992)
Penrith D	0.046	0.1	101.2	87.9	0.87	H & M (1992)
Penrith E	0.115	6.2	59.7	40.8	0.68	H & M (1992)
Redcliffe	-	3.2	36.1	22.4	0.62	H & M (1992)
Midford Sands	0.156	1.7	23.2	14.6	0.63	H & M (1992)
Ardingly Sandstone A	0.19	4.9	42.2	36.9	0.87	H & M (1992)
Ardingly Sandstone B	0.173	8.9	53.4	47.6	0.89	H & M (1992)
Ashdown Sandstone	0.201	0.4	30.6	32.3	1.06	H & M (1992)
Greensand A	0.383	50.5	10.5	2.3	0.22	H & M (1992)
Greensand A Dogger	0.173	16.9	74.5	46.7	0.63	H & M (1992)
Chatsworth Grit	0.146	-	39.2	24.3	0.62	Bell (1995)
Sherwood Sandstone	0.257	-	11.6	4.8	0.41	Bell (1995)
Keuper Waterstone	0.101	-	42.0	28.6	0.68	Bell (1995)
Bronllwyn Grit	0.018	-	197.5	190.7	0.97	Bell (1995)
Sneinton Formation sandstone	0.163	11.0	23.7	14.1	0.60	Bell and Culshaw (1998)
Sneinton Formation sandstone	0.178	14.0	26.1	16.2	0.62	Bell and Culshaw (1998)
Sneinton Formation sandstone	0.18	6.0	25.2	16.8	0.67	Bell and Culshaw (1998)
Sneinton Formation sandstone	0.182	7.0	27.6	19.6	0.71	Bell and Culshaw (1998)
Sneinton Formation sandstone	0.167	4.0	26.4	20.1	0.76	Bell and Culshaw (1998)
Sneinton Formation sandstone	0.163	10.0	32.5	17.6	0.54	Bell and Culshaw (1998)
Sneinton Formation sandstone	0.19	5.0	24.4	13.7	0.56	Bell and Culshaw (1998)
Sneinton Formation sandstone	0.186	12.0	28.0	20.5	0.73	Bell and Culshaw (1998)
Sneinton Formation sandstone	0.166	6.0	17.4	10.7	0.62	Bell and Culshaw (1998)
Sneinton Formation sandstone	0.187	6.0	39.8	25.6	0.64	Bell and Culshaw (1998)

Sneinton Formation sandstone	0.181	12.0	30.9	24.9	0.81	Bell and Culshaw (1998)
Penrith sandstone	0.28	5.0	28.4	9.37	0.33	Cuss et al. (2003)
Darley Dale sandstone	0.135	6.0	44.4	37.7	0.85	Cuss et al. (2003)
Tennessee (Crab Orchard) sandstone	0.075	10.0	89.9	69.4	0.77	Cuss et al. (2003)
Tertiary sandstone (Taiwan) (WGS1)	0.174	21.3	34.1	25.4	0.75	Lin et al. (2005)
Tertiary sandstone (Taiwan) (WGS2)	0.167	69.6	47.5	6.7	0.14	Lin et al. (2005)
Tertiary sandstone (Taiwan) (MS1)	0.115	43.1	48.5	28.9	0.60	Lin et al. (2005)
Tertiary sandstone (Taiwan) (MS2)	0.141	21.5	37.1	28.3	0.76	Lin et al. (2005)
Tertiary sandstone (Taiwan) (MS3)	0.131	41.3	82.7	43.3	0.52	Lin et al. (2005)
Tertiary sandstone (Taiwan) (TL1)	0.131	58.1	68.7	23.2	0.34	Lin et al. (2005)
Tertiary sandstone (Taiwan) (TL2)	0.128	42.7	77.5	44.2	0.57	Lin et al. (2005)
Tertiary sandstone (Taiwan) (ST)	0.182	50.6	38.4	7.8	0.20	Lin et al. (2005)
Tertiary sandstone (Taiwan) (NK)	0.148	66.4	86.0	43.2	0.50	Lin et al. (2005)
Tertiary sandstone (Taiwan) (TK)	0.128	67.7	69.0	29.4	0.43	Lin et al. (2005)
Tertiary sandstone (Taiwan) (SFG1)	0.246	30.2	14.5	12.2	0.84	Lin et al. (2005)
Tertiary sandstone (Taiwan) (SFG2)	0.169	48.6	46.4	19.9	0.43	Lin et al. (2005)
Tertiary sandstone (Taiwan) (CL)	0.207	50.4	19.9	3.1	0.16	Lin et al. (2005)
Balatonrendes sandstone (Hungary)	0.042	-	45.7	35.0	0.77	Vásárhelyi and Ván (2006)
Cserkút sandstone (Hungary)	0.018	-	78.6	61.4	0.78	Vásárhelyi and Ván (2006)
Pilisborosjenõ sandstone (Hungary)	0.135	-	20.4	17.7	0.87	Vásárhelyi and Ván (2006)
Vác sandstone (Hungary)	0.121	-	33.8	25.2	0.75	Vásárhelyi and Ván (2006)
Bad Bentheim (perp)	0.233	6	50.4	49.4	0.98	Demarco et al. (2007)
Bad Bentheim (para)	0.233	6	50.2	49.5	0.99	Demarco et al. (2007)
Bebertal (perp)	0.09	1	92.8	58.2	0.63	Demarco et al. (2007)
Bebertal (para)	0.09	1	75.8	42.2	0.56	Demarco et al. (2007)
Obernkirchen (perp)	0.264	6	64.4	55.2	0.86	Demarco et al. (2007)
Obernkirchen (para)	0.264	6	55.6	48.0	0.86	Demarco et al. (2007)

Sander (perp)	0.147	5	70.7	37.5	0.53	Demarco et al. (2007)
Sander (para)	0.147	5	64.0	32.7	0.51	Demarco et al. (2007)
Schleeriether (perp)	0.142	2	84.4	43.5	0.52	Demarco et al. (2007)
Schleeriether (para)	0.142	2	69.3	34.3	0.50	Demarco et al. (2007)
Tambach (perp)	0.084	1	204.6	194.6	0.95	Demarco et al. (2007)
Tambach (para)	0.084	1	179.4	140.0	0.78	Demarco et al. (2007)
Weser grau (perp)	0.094	1	164.8	136.5	0.83	Demarco et al. (2007)
Weser grau (para)	0.094	1	153.4	133.2	0.87	Demarco et al. (2007)
Weser rot (perp)	0.063	2	145.5	94.9	0.65	Demarco et al. (2007)
Weser rot (para)	0.063	2	154.0	104.8	0.68	Demarco et al. (2007)
Los Alambres sandstone (Salamanca, Spain)	0.145	-	36.0	19.7	0.55	Nespereira et al. (2010)
Matagrillos sandstone (Salamanca, Spain)	0.119	-	23.0	15.8	0.69	Nespereira et al. (2010)
Arapiles A-1-1 sandstone (Salamanca, Spain)	0.103	-	58.1	42.1	0.72	Nespereira et al. (2010)
Arapiles A-2-1 sandstone (Salamanca, Spain)	0.133	-	177.6	162.9	0.92	Nespereira et al. (2010)
Arapiles A-2-2 sandstone (Salamanca, Spain)	0.088	-	119.4	109.1	0.91	Nespereira et al. (2010)
Cotta-type Elbe sandstone (LG XI)	0.199	2.7	40.5	31.7	0.78	Siedel (2010)
Cotta-type Elbe sandstone (LG 12)	0.239	3.3	29.4	20.6	0.70	Siedel (2010)
Cotta-type Elbe sandstone (LG 14)	0.274	2.1	30.5	20.3	0.67	Siedel (2010)
Cotta-type Elbe sandstone (LG 15)	0.267	2.4	31.6	24.1	0.76	Siedel (2010)
Cotta-type Elbe sandstone (LG 16)	0.22	3.3	33.2	18.7	0.56	Siedel (2010)
Cotta-type Elbe sandstone (LG XVII)	0.21	4.7	39.7	17.7	0.45	Siedel (2010)
Cotta-type Elbe sandstone (Neu 21)	0.22	4.8	21.1	18.9	0.90	Siedel (2010)
Cotta-type Elbe sandstone (Neu 22)	0.23	3.1	19.8	15.8	0.80	Siedel (2010)
Cotta-type Elbe sandstone (Neu Co)	0.192	4.8	45.0	26.5	0.59	Siedel (2010)
Cotta-type Elbe sandstone (UK 12/1)	0.224	2.9	51.8	41.6	0.80	Siedel (2010)

Cotta-type Elbe sandstone (UK 12/2)	0.223	3.4	39.2	28.6	0.73	Siedel (2010)
Cotta-type Elbe sandstone (OK 13/1)	0.229	3.0	43.0	32.9	0.77	Siedel (2010)
Cotta-type Elbe sandstone (Pow 15/1)	0.221	2.4	45.6	43.1	0.95	Siedel (2010)
Cotta-type Elbe sandstone (Hor 16/1)	0.213	2.5	47.8	43.9	0.92	Siedel (2010)
Cotta-type Elbe sandstone (RD A)	0.262	3.1	31.0	25.6	0.83	Siedel (2010)
Cotta-type Elbe sandstone (RD B)	0.234	3.1	46.2	34.8	0.75	Siedel (2010)
Cotta-type Elbe sandstone (RD C)	0.222	2.0	56.9	50.7	0.89	Siedel (2010)
Posta-type Elbe sandstone (ML 1)	0.194	1.8	64.6	65.7	1.02	Siedel (2010)
Posta-type Elbe sandstone (ML 2)	0.217	1.3	51.3	58.2	1.14	Siedel (2010)
Posta-type Elbe sandstone (ML 3)	0.225	1.6	51.4	52.7	1.03	Siedel (2010)
Posta-type Elbe sandstone (Her H)	0.21	0.0	57.6	45.6	0.79	Siedel (2010)
Posta-type Elbe sandstone (Her II)	0.208	1.2	55.1	50.8	0.92	Siedel (2010)
Posta-type Elbe sandstone (Her III)	0.222	1.5	53.2	45.2	0.85	Siedel (2010)
Posta-type Elbe sandstone (Her IV)	0.193	1.1	54.8	43.6	0.80	Siedel (2010)
Posta-type Elbe sandstone (Her V)	0.217	1.5	45.0	47.6	1.06	Siedel (2010)
Posta-type Elbe sandstone (Zei 6/1)	0.22	0.8	58.2	49.2	0.85	Siedel (2010)
Posta-type Elbe sandstone (Zei 6/2)	0.226	0.0	58.8	53.8	0.92	Siedel (2010)
Posta-type Elbe sandstone (Zei 6/3)	0.228	0.9	53.1	45.5	0.86	Siedel (2010)
Posta-type Elbe sandstone (Zei 6/4)	0.228	0.8	53.8	48.4	0.90	Siedel (2010)
Posta-type Elbe sandstone (OV 7/1)	0.234	1.0	43.5	44.0	1.01	Siedel (2010)
Posta-type Elbe sandstone (OV 7/2)	0.186	1.5	75.9	62.7	0.83	Siedel (2010)
Posta-type Elbe sandstone (Mo 8/1)	0.204	0.6	46.1	42.2	0.92	Siedel (2010)
Posta-type Elbe sandstone (Mo 8/2)	0.196	0.9	55.6	53.5	0.96	Siedel (2010)
Posta-type Elbe sandstone (Sch 9/1)	0.242	0.8	37.1	37.9	1.02	Siedel (2010)
Posta-type Elbe sandstone (Sch 9/2)	0.231	1.0	43.8	37.3	0.85	Siedel (2010)
Posta-type Elbe sandstone (OK 13/2)	0.229	1.6	53.2	45.4	0.85	Siedel (2010)

Posta-type Elbe sandstone (WB 14/1)	0.229	0.7	50.3	41.2	0.82	Siedel (2010)
Posta-type Elbe sandstone (WB 14/2)	0.237	1.3	50.5	41.4	0.82	Siedel (2010)
Posta-type Elbe sandstone (Pow 15/2)	0.251	1.2	36.9	22.4	0.61	Siedel (2010)
Posta-type Elbe sandstone (Gri 17/1)	0.214	0.4	57.8	57.6	1.00	Siedel (2010)
Grampians sandstone (10° angle)	0.09	6.2	59.7	50.4	0.84	Wasantha et al. (2014)
Grampians sandstone (20° angle)	0.09	6.2	58.8	47.0	0.80	Wasantha et al. (2014)
Grampians sandstone (35° angle)	0.09	6.2	53.7	46.5	0.87	Wasantha et al. (2014)
Grampians sandstone (55° angle)	0.09	6.2	45.9	39.8	0.87	Wasantha et al. (2014)
Grampians sandstone (83° angle)	0.09	6.2	57.4	49.7	0.87	Wasantha et al. (2014)

949